# HYBRID ADJUSTMENT OF UAS-BASED LiDAR AND IMAGE DATA

YOGENDER
June 2022

SUPERVISORS:
Dr. Bashar Alsadik (ITC-EOS)
Dr. Francesco Nex (ITC-EOS)

SCIENTIFIC ADVISOR:
Dr. Fabio Remondino
Bruno Kessler Foundation (FBK),
Trento, Italy

EXTERNAL ADVISOR:
Dr. Philipp Glira
Austrian Institute of Technology (AIT),
Vienna, Austria

# Hybrid adjustment of UAS-based LiDAR and image data

YOGENDER
Enschede, The Netherlands, June 2022

Thesis submitted to the Faculty of Geo-Information Science and Earth Observation of the University of Twente in partial fulfilment of the requirements for the degree of Master of Science in Geo-information Science and Earth Observation.
Specialization: Geoinformatics

SUPERVISORS:
Dr. Bashar Alsadik (ITC-EOS)
Dr. Francesco Nex (ITC-EOS)

SCIENTIFIC ADVISOR:
Dr. Fabio Remondino
Bruno Kessler Foundation (FBK),
Trento, Italy

EXTERNAL ADVISOR:
Dr. Philipp Glira
Austrian Institute of Technology (AIT),
Vienna, Austria

THESIS ASSESSMENT BOARD:
Prof. dr. ir. M.G. Vosselman (Chair)
drs. Wan Bakx ( Procedural advisor)
Dr. Mila Koeva, ITC-PGM (External Examiner)

*This M.Sc. thesis is dedicated to my mother, Saroj Devi, and my father, Vijender Singh Yadav.*

Throughout all thick and thin, I have always believed and motivated by this line from my sister,

*"You will go farther than what you think."*

- Mansi Nagpal

# ABSTRACT

Several advancements are going with Unmanned Aerial Systems (UAS) with the addition of multiple sensors and simultaneous data acquisition to obtain detailed geo-data for various applications. However, simultaneous data acquisition with multiple sensors, namely camera, and LiDAR, will also result in possible discrepancies associated with them. These discrepancies must be solved to use a reliable and accurate final product.

This research aimed to minimize the discrepancies/errors between the LiDAR and the image data acquired simultaneously with an Unmanned Aerial Systems (UAS) by implementing a hybrid adjustment approach. There can be several discrepancies associated with both the datasets due to the different characteristics of the sensors and the terrain conditions. The initial trajectory of the UAS, raw LiDAR measurements, and image observations were the inputs used for the hybrid adjustment. The UAS trajectory, LiDAR strips, intrinsic calibration of Lidar and camera sensors, and exterior orientations of the images were adjusted and estimated correctly in this hybrid adjustment approach. After hybrid adjustment, both LiDAR and camera-based point clouds are expected to be in the same reference system, with minimal discrepancies between them. In this hybrid adjustment workflow, the discrepancies were minimized with a least-squares-based simultaneous adjustment for both LiDAR and image datasets. For the hybrid adjustment process, three types of correspondences were established, namely: between image pairs (IMG-to-IMG), between LiDAR strips (STR-to-STR), and between image and LiDAR strips (IMG-to-STR). The hybrid adjustment process was experimented with coupled images (coupled to a common LiDAR/image trajectory by the time stamp of images), loose images (not tied to a common LiDAR/image trajectory), and raw LiDAR measurements. We have also experimented with the UAS trajectory correction with bias and linear trajectory correction models in the hybrid adjustment process. After each iteration of hybrid adjustment, a convergence criterion is tested (relative change of the weighted sum of squared errors), and a new iteration cycle starts until a given number of iterations are completed. After hybrid adjustment, a Dense Image Matching (DIM) point cloud was generated with Pix4DMapper using the undistorted images and estimated image orientations from the hybrid adjustment without further optimization of the orientations. For quality control, the relative height difference between the LiDAR and DIM point clouds and Cloud-to-Cloud distances were compared between both the point clouds before and after hybrid adjustment. We also carried out the surface-level analysis of the results to better interpret the errors before and after hybrid adjustment.

From the results, it was observed that the most accurate orientation between LiDAR and image data could be obtained by implementing the hybrid adjustment with coupled images and a bias trajectory correction model. It was observed that the alignment between the point clouds has significantly improved from the range of meters to a sub-centimeter level after implementing the hybrid adjustment process.


**Keywords**: Unmanned Aerial Systems, LiDAR, hybrid adjustment, point clouds, UAS trajectory.

# ACKNOWLEDGEMENTS

From the depth of my heart, I would like to thank my supervisors, Dr. Bashar Alsadik and Dr. Francesco Nex, under whose guidance I have accomplished my research goals. They have supported me in developing my overall scientific knowledge for the research. Their immense support, guidance, and continuous motivation throughout my M.Sc. research are highly acknowledged.

I would also like to express my gratitude to Dr. Fabio Remondino for his valuable input and for providing me with the required datasets for the research. Next, I want to thank Dr. Philipp Glira for his valuable time and support in implementing the hybrid adjustment process. Without the support of supervisors and advisors, it would have been impossible for me to perform my research. I am always grateful to all of them.

I am also thankful to Prof. George Vosselman for his valuable time in assessing my research proposal and thesis document.

Thank you, Mr. Wan Bakx, for your immense support and guidance in the research proposal writing and for your time in all the research assessment presentations.

I am highly grateful to Mr. Wilfried Karel and everyone from team Opals, Technical University in Wien, for providing me with a scientific license key to use Opals to implement hybrid adjustment for my research.

I would also like to thank Dr. Mahesh Pal, Professor, National Institute of Technology (NIT), Kurukshetra, India, who has been a constant inspiration for me. He is the one who guided me in the field of remote sensing during my bachelor's studies. I am always indebted to you, sir.

My special thanks to Dr. Martin Mokros from Technical University in Zvolen, Slovakia, who guided me during the internship and helped me develop an attentive and critical attitude toward the research. He also helped improvise the presentation skills to communicate the ideas to the audience effectively. I would also like to thank Mrs. Mariana from TU Zvolen, Slovakia, for her lessons and support during the M.Sc. research phase.

I cannot forget to thank the Faculty ITC and the University of Twente for providing me the financial support for my master's studies with the ITC Excellence Scholarship. I am highly thankful for it.

Thanks to my seniors from Faculty ITC, Ranit De and Dhananjay Umalkar, who guided and supported me during my studies and research.

I can never forget the support from my family and friends during some of the struggling phases of the research. I am indebted to my parents, grandparents, and sisters, Neha, and Mansi, who always helped me remain calm and focused in all situations. A special mention to my friends Arvind Gauns, Prashant Pandit, Srikumar Sastry, Girma Tsige, Anmol Popli, and Ishank Bhardwaj for always lifting my spirits during all the times of my tenure at Faculty ITC.

Yogender
Enschede, Netherlands
11-June-2022

# TABLE OF CONTENTS

# LIST OF FIGURES

# LIST OF TABLES

# LIST OF ABBREVIATIONS

| | |
|---|---|
| 3DIS | 3D Imaging Systems |
| C2C | Cloud-to-Cloud distance |
| CPC | Control Point Cloud |
| DIM | Dense Image Matching |
| DSM | Digital Surface Model |
| GCP | Ground Control Point |
| GNSS | Global Navigation Satellite Systems |
| HOG | Histogram of oriented gradients |
| ICP | Iterative Closest Point |
| IMG-IMG | Correspondence between Image pairs |
| IMG-STR | Correspondence between Image tie points and LiDAR strip |
| IMU | Inertial Measurement Unit |
| INS | Inertial Navigation System |
| LiDAR | Light Detection and Ranging |
| OPALS | Orientation and Processing of Airborne Laser Scanning data |
| QC | Quality Check |
| SCS | Scanner Coordinate System |
| SIFT | Scale-Invariant Feature Transform |
| SfM | Structure from Motion |
| STR-STR | Correspondence between LiDAR strips |
| UAS | Unmanned Aerial Systems |

# 1. INTRODUCTION

The purpose of this chapter is to frame an outline for the research problem that has been addressed in this M.Sc. research work with the subsections research problem, research gap, scientific relevance, and finally, the practical applicability of the research work

## 1.1. Motivation for the research topic

In the last decade, there have been significant advancements in the Unmanned Aerial System (UAS) based data acquisition. With UAS-based multi-sensor data acquisition, different sensors give earth observation datasets in various formats. For example, camera sensors give RGB images with pixel-level information, whereas Light Detection and Ranging (LiDAR) sensors provide geometrical details of all the points in the point cloud output. LiDAR point cloud and camera imagery are the primary data sources in remote sensing and photogrammetry. They have their unique data characteristics, making them preferable for specific applications. Data coregistration is an efficient technique to utilize both data sources simultaneously (Zhang & Lin, 2017). It improves the output values, increases the interpretation performance of the data source, and results in the enhanced quality representation of the visual data (Zhang, 2010). The advantage of the data product obtained from the integration is that the output generated is more accurate and includes minute details from the received datasets. Many scientific experiments have been carried out to coregister multi-sensor datasets accurately to get detailed and enriched information; still, there is a need for a robust, simplified, and automated solution for UAS-based multi-sensor data coregistration. The dual advantage of pixel-level and geometrical information can be used from a precisely coregistered UAS-based camera and LiDAR datasets.

## 1.2. Research Problem

The point cloud coregistration is one of the vital steps in integrating datasets from LiDAR and camera sensors after the data acquisition and initial processing. Coregistration is the step for unifying the point clouds from dual sensors to get a single product with minimal errors to fetch the dual advantage from a single point cloud. Many misalignments and distortions have been observed in the coregistration of 3D point clouds obtained from LiDAR data and camera images acquired simultaneously with a multi-sensor Unmanned Aerial Systems (UAS).

The LiDAR point cloud and the derived point cloud from camera images have some misalignments during their coregistration due to the systematic errors in the multi-sensor UAS system. The primary source of these systematic errors are GNSS/INS navigation systems and the boresight alignment from mounting calibration (Philipp Glira, 2018). Figure 1.1 shows the misalignment between two different point clouds in red and green colors where there is a displacement between two-point clouds for a similar feature (highlighted in a red window).

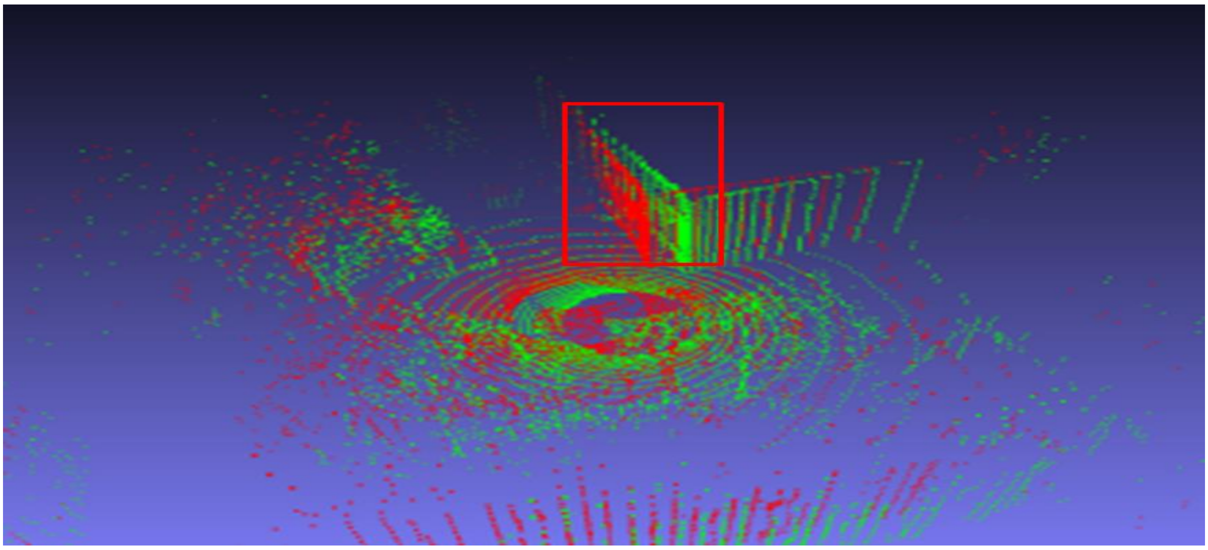

Figure 1.1: Representation of the misalignment in the two-point clouds (Almqvist et al., 2018)

These misalignments and distortions compromise the coregistration quality of the datasets. The discrepancies between two-point clouds can be attributed to different data acquisition sensors and their characteristics. It is not easy to get a highly accurate coregistration between LiDAR point clouds and point clouds obtained from the processing of camera imagery data using only hardware synchronization and bore-sight calibration (J Skaloud, 2006). The initial UAS trajectory data also needs to be considered for the precise coregistration of both datasets. This research aims to apply a hybrid adjustment approach to minimize the discrepancies between the point clouds from UAS-based LiDAR and camera data.

## 1.3. Research Gap

The initial discrepancies in coregistration between point clouds from LiDAR and camera datasets can range up to several decimeters or more (Cucchiaro et al., 2020). After data acquisition and processing, no rigorous and simplified solution exists for an accurate co-registration of the UAS-based LiDAR and camera datasets. Some preprocessing optimization steps, namely LiDAR strip adjustment and aerial triangulation, exist, but discrepancies can arise after solving these two optimization problems separately (Philipp Glira, 2018). To solve this geometric state of art problem, many strategies exist to minimize the discrepancies between the LiDAR and camera datasets, but very few focus on the simultaneous adjustment of both LiDAR and camera datasets. The minimization of the coregistration error considering the raw LiDAR measurements, the initial trajectory of the UAS, and constraining the correspondences matching to the limited number of points from both LiDAR and camera has still much scope to explore. This M.Sc. research aims to apply the hybrid adjustment method considering the raw LiDAR measurements from the scanner, initial UAS trajectory, and correspondence establishment using the selected points from both the datasets to minimize the discrepancies between LiDAR and camera datasets.

## 1.4. Scientific Relevance

The technical progressions in UAS-based sensor technology and data acquisition have led to the emergence of high-resolution data availability. The multi-sensor platform-based applications are highly flexible for data acquisition (Wei, 2017). The different sensors, namely LiDAR and camera, are emerging technologies for 3D topographic mapping (Philipp Glira, 2018), especially when used onboard UAS platforms. The LiDAR point cloud provides accurate 3D surface information in the form of the scattered point cloud, whereas aerial photogrammetry provides information through stereo vision directly in the form of spectral imagery (Yang & Chen, 2015).

During the last decade, the applications of the UAS-based LiDAR technique combined with camera imagery have provided accurate and precise geometric information on the terrain features. LiDAR data is limited in detecting the sudden elevation changes due to low points, i.e., object-space break-lines (Kumar Mishra, 2012). The optical imagery compliments this by providing high-quality details along the object boundaries with variations in elevation (Kim et al., 2006). In the case of LiDAR and camera data acquisition, the strength in the one compliments the limitation of the other technique. Hence, combining the data from both these techniques would give us accurate, high-quality, and detailed surface information(Baltsavias, 1999). Accurate coregistration of UAS-based camera images and LiDAR data can positively influence several applications in the sector of mapping, 3D city modelling, and many more.

### 1.5. Practical applications of the research

The integration of datasets from different sensors has been relevant for many applications in agriculture, infrastructure, forestry, archaeology, building feature extraction, city modeling, structural damage modeling, and many more (Lin & Habib, 2021; Ribeiro, 2021; Vilbig et al., 2020; Wallace et al., 2012). The integrated product from LiDAR and camera imagery also finds its applications in high-resolution datasets in natural disaster management (Gomez & Purdie, 2016). The datasets with detailed information can be employed to develop urban infrastructure planning projects. The urban accessibility and expansion can also be explored using the integrated datasets from LiDAR and aerial photogrammetry in building extraction, image classification, city modeling, and structural damage mapping (Kerle et al., 2020; Pandey et al., 2016).

Fully integrated UAS-based LiDAR and imagery mapping sensors are available in the market for utility-grade, survey-grade, and multi-purpose grade mapping usages. True View 3D Imaging Systems (3DIS), shown in Figure 1.3, are one of the advanced multi-sensor data acquisition systems used for a full range of diverse applications in mining, infrastructure, construction, oil and gas, and land development (GeoCue Group, 2021). Other data acquisition systems like IGI systems (Figure 1.2) and Leica City Mapper (Figure 1.4) are also used in mapping applications. The suggested hybrid adjustment approach can be used in the coregistration of the datasets from these data acquisition systems for a detailed product.


Figure 1.2: IGI systems (IGI Systems, 2022)

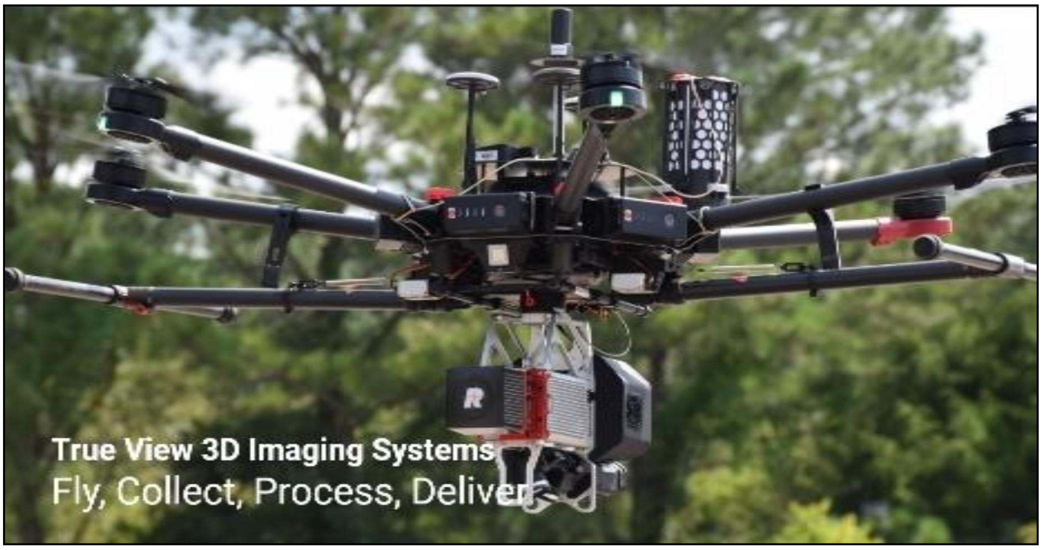


Figure 1.3: True View 3D Imaging Systems (GeoCue Group, 2021)


Figure 1.4: Leica City Mapper (Leica Geosystems, 2022)

Such 3DIS can be mounted on any UAS system, and they collect high-quality LiDAR and imagery data in a single flight followed by processing in dedicated software. It enables the fast, easy automated generation of accurate 3D colorized point clouds, oblique imagery, and orthophotos from a single UAS flight (GeoCue Group, 2021). A multi-sensor remote sensing system can help us gather rich information about the scanned objects on the ground surface.

Although the existing 3DIS systems provide the LiDAR and imagery data from a single flight, they lack the integrated product from both the sensors. The proposed hybrid adjustment workflow can be adopted for the datasets acquired from these 3DIS systems, making them more efficient for data integration. The integrated dataset will open the door for broad remote sensing applications in earth observations like object detection, mapping, agriculture, and many others. Investment in data integration technologies will help to enhance the data quality and extract accurate information from the desired area.

## 1.6. Contributions of the research

This M.Sc. research is focused on applying a hybrid adjustment approach for UAS-based LiDAR and image data, which is expected to minimize their coregistration error between both datasets. It is worth mentioning that the central methodology and mathematical framework for this M.Sc. research work were adopted from the Ph.D. work presented by Dr. Philipp Glira (Philipp Glira, 2018), further considering different constraints, adjusted weights, optimal processing parameters, and results analysis for UAS-based LiDAR and camera datasets. The significant contributions from this research are:

- Raw measurements from LiDAR, camera images, and trajectory inputs from the UAS-based LiDAR system were used for the simultaneous adjustment of the orientation of UAS-based LiDAR strips and image data
- Optimization of the relative height differences between datasets before and after hybrid adjustment
- Comparison of 3D point distances between the camera and LiDAR-based point clouds before and after hybrid adjustment

## 1.7. Innovative elements of the research

The novelty of this M.Sc. research is to apply the existing hybrid adjustment approach for UAS-based LiDAR and image datasets, investigating the influence of multiple parameters on the results after the adjustment. The unique elements in this M.Sc. research work are:

- Raw measurements from the LiDAR scanner (.rdbx files) in Scanner Coordinate System (SCS) were used for the hybrid adjustment instead of "las" files post-processing in software.
- Criteria for the roughness and threshold angle between surface normals have been used in hybrid adjustment to select correspondences accurately.
- Instead of using Correspondences between LiDAR and image data from the entire dataset area, the hybrid adjustment was guided with the correspondences limited to the planar and smoother surfaces,
- Instead of using all the points from the datasets for the correspondences, query points (subset) were selected with a uniform sampling technique.
- Parameter tuning was done through multiple experiments for the hybrid adjustment for the UAS-based camera and LiDAR datasets.
- 3D cloud-to-cloud distances between LiDAR and camera-based point clouds were computed for the primary quality check of the hybrid adjustment.
- The methodology workflow from the pre-processing of the datasets to the quality check after hybrid adjustment is developed for UAS-based LiDAR and image datasets.

## 1.8. Objective of the research

### 1.8.1. Overall objective of the research

To apply an end-to-end hybrid adjustment approach to minimize the discrepancies between the LiDAR and image data acquired simultaneously from a UAS platform.

#### 1.8.2. Sub-objectives of the research

1. To pre-process and prepare the UAS-based camera and LiDAR data for the hybrid adjustment.
2. To define an efficient end-to-end methodology for the hybrid adjustment of UAS-based LiDAR and camera data.
3. To investigate the suitable types of correspondences which can be used for the hybrid adjustment with UAS-based LiDAR and image datasets.
4. To study the effect of the UAS trajectory correction on the hybrid adjustment results with bias and linear trajectory correction models.
5. To use the subset of datasets to establish the correspondences in the hybrid adjustment process with a uniform point sampling technique.
6. To implement a hybrid adjustment methodology with loose and coupled images and perform the quality checks of the results after hybrid adjustment.

### 1.9. Research Questions

1. What is the hybrid adjustment process, and what inputs and optimal parameters need to be considered for the hybrid adjustment of UAS-based LiDAR and image data?
2. What are loose and coupled images, and what is their role in the implementation of the hybrid adjustment process?
3. Which types of correspondences are established, and how are they established in the hybrid adjustment process?
4. What constraints can be applied to the establishment of the correspondence in the hybrid adjustment approach, and how do these constraints affect the hybrid adjustment process?
5. How does a trajectory correction model affect the hybrid adjustment process, and where does it play its role?
6. Can the discrepancies be impacted by implementing the hybrid adjustment with loose and coupled images, and to what extent are they impacted?

### 1.10. Outline of the research

This M.Sc. research thesis is divided into eight chapters. Chapter 1 provides an introduction, relevance, and applications of the research. Chapter 2 describes the comprehensive state-of-the-art methods developed so far for the multi-sensor UAS-based data integration. Chapter 3 elaborates on the study area and dataset acquisition systems. Chapters 4 and 5 describe the methodological framework and workflow, respectively. Finally, Chapter 6 presents the results and analysis of the implementation of the hybrid adjustment process, followed by the conclusive remarks and recommendations in Chapter 7. Ethical considerations have been summarized in Chapter 8.

# 2. STATE OF THE ART

This chapter provides a glimpse of the data acquisition with multi-sensor UAS and state-of-the-art methods that have been developed so far to minimize the error between the camera and LiDAR datasets. It also gives an overview of the recent developments related to the undertaken M.Sc. research. The last section of this chapter also highlights the research articles related to the hybrid adjustment.

## 2.1. Data acquisition with multi-sensor UAS systems

The low-cost small UAS system varying in sensors mounted on them and level of autonomy has been recently developed for multi-purpose data acquisition (G. Zhou & Reichle, 2010). A typical UAS system has an integrated GPS and a sensor board with different sensors mounted depending on the purpose of data acquisition. The independent sensor units like the RGB camera, Multispectral camera, and LiDAR system can also be attached to a UAS system for the data acquisition. Figure 2.1 shows a multi-sensor UAS system for simultaneous collection from camera and LiDAR sensors.

Figure 2.1: A multi-sensor UAS-system equipped with LiDAR and camera sensors for simultaneous data acquisition (YellowScan, 2020)

The simultaneous acquisition of geo-data from multiple sensors onboard an UAS-platform has increased the efficiency of the data collection, and their coregistration would further contribute to it. Despite their limited payload capability, the integration of data collected from multi-sensor UAS is increasing due to downscaling of the sensors in terms of weight and volume. The acquisition of data from UAVs with a multi-sensor system onboard enables the fusion of LiDAR and imagery point clouds complementing each other's characteristics and resulting in a detailed and optimized product (Mandlburger et al., 2017).

## 2.2. UAS Photogrammetry and LiDAR

3D reconstruction in aerial photogrammetry is based on the principle of the intersection of rays, e.g., for a single point; reconstruction requires a minimum of two intersecting rays from two images at different locations indicating the same point. Extrinsic parameters of an image define single image characteristics ({X, Y, Z}, omega, phi, kappa), and intrinsic parameters of an image are principal point, image size, focal length, and distortion parameters (Gerum et al., 2019; MATLAB, 2021). The imagery's exterior and interior orientation parameters can be determined from the redundancy contained in the overlap in the images and validated with the ground-truth data (GCPs or control point clouds). The exterior orientation parameters can be estimated by combining the flight trajectory from GNSS/INS and camera mounting calibration. Aerial triangulation of imagery has many similarities with the strip adjustment of the LiDAR strip; still, both these steps are carried out independently in practice. Over the last decades, these orientation problems have been intensely studied, and advanced models exist for aerial triangulation (Förstner & Wrobel, 2016) and LiDAR strip adjustment (Jie Shan, 2018).

Numerous studies have been carried out to reconstruct the 3D surfaces using LiDAR data and aerial photogrammetry simultaneously due to their complementary characteristics (Ayman Habib et al., 2005). The main advantage of using the LiDAR system is the direct acquisition of the 3D coordinates from the ground objects and the better vertical positional accuracy when using an airborne platform. In contrast, camera images provide dense spatial information with better horizontal accuracy (Choi et al., 2011). The datasets acquired from the UAS-based LiDAR system have low-cost, denser point clouds and shorter response times than traditional aircraft or helicopter-based LiDAR data acquisition (Nex et al., 2022). The combined advantage of LiDAR data and images can be fully utilized after eliminating geometric inconsistency between both datasets, i.e., geometric registration, which arises due to the systematic errors of a multi-sensor system (Kim et al., 2006).
Figure 2.2 shows the data acquisition from a UAS-platform with photogrammetry (left) and LiDAR (on the right)

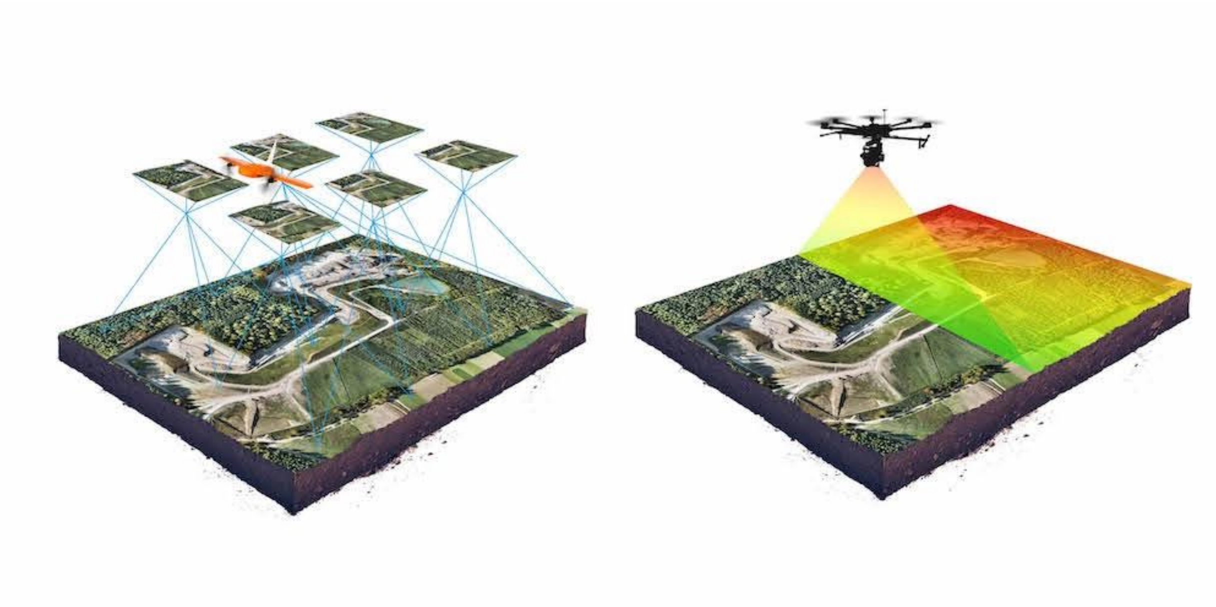

Figure 2.2: Data acquisition from UAS photogrammetry (left) and UAS LiDAR (right) (Moasaic, 2022)

The point clouds from UAS-photogrammetry have two main advantages a) higher point density as a 3D point cloud is reconstructed considering every image pixel, and b) RGB information of every point in the point cloud (Fritz et al., 2013). In complement to this, the LiDAR point cloud's accuracy is reliable in the case of occlusions and areas with sudden elevation variations. Also, less noisy data and the multi-echo/multi returns information from vegetation characteristics add value to LiDAR data.

## 2.3. Synchronization issues between multi-sensor-based data acquisition

Coregistration of the geodata is required when data is collected for the exact location using different sensors on a platform. The primary source of the errors between multi-sensor datasets is the different data acquisition characteristics of the sensors and their different coordinate system. Although, they can be brought to a similar coordinate system by using ground truth data, possibly resulting in discrepancies. The displacements in the spatial separation between the sensors (lever-arm) and boresight calibration for multiple sensors also contribute to the discrepancies in the UAS-based multi-sensor datasets. The geo-data must be in the same coordinate system for further dataset processing as due to improper coregistration, errors are introduced in the obtained dataset. The errors in the dataset can further affect the classification of objects (Haklay & Weber, 2008) and the reliability of the final products. The dataset obtained from various sensors and different resolutions influences the quality of the data acquisition. The available georeferenced data from the different geo-databases also contributes to the distortion during data fusion. Still, a margin of coregistration ranges from decimeters to centimeters depending upon the algorithm employed (Cucchiaro et al., 2020). The well-known Iterative Closest Point (ICP) algorithm registers point clouds generated from LiDAR and imagery at various processing steps. LiDAR data and imagery can integrate well if they are precisely registered to optimize the geometrical errors arising from two datasets (Peng et al., 2019).

## 2.4. Coregistration methods developed so far

The two primary approaches for registering multi-sensor datasets, especially LiDAR and camera, can be classified as area-based registration and feature-based registration (Palenichka & Zaremba, 2010). Area-based registration methods focus on optimizing exterior orientation parameters of the images by maximizing the statistical or grayscale comparations of the similar area in both datasets. On the other hand, data-driven feature-based fusion approaches perform the integration by fetching out the features from LiDAR and images to generate correspondences to estimate the camera poses. To generalize, the area-based registration approaches are based on the statistical dependence of LiDAR and imagery and are mainly dependent on the quality and correctness of image intensity which is interpreted with intensity calibration effectiveness (Yang & Chen, 2015). However, the feature-based method extracts geometric features from a scene to register the datasets (T. Zhou et al., 2021). Generally, the methods used for extracting the features from the datasets depend on the characteristics of the individual source data, which can vary if different datasets are used. The use of multi-sensor platforms with a LiDAR unit and a single/multi-view camera for synchronized data acquisition has represented a market trend for the 3D reconstruction of the earth's surface (Toschi et al., 2018). There are numerous supporting reasons for the applications of multi-sensor data, including the complementary characteristics of two sensors and the detailed multispectral information offered in combination with photogrammetry (Toschi et al., 2021). Their use is limited to the concurrent flights and finds their place in exploring the fusion of data collected at different timestamps.

(Ressl et al., 2016) compared point clouds from Dense Image Matching (DIM) and LiDAR stating concern on the capability of retrieving ground data (DTMs). This work also focused on the point that the height of the points from LiDAR can be lower concerning triangulate image points due to the penetration capability of the LiDAR scanner. Many potential research works have been carried out for the combined processing of LiDAR and imagery to get a detailed and accurate end product, e.g., an integrated approach to generate the orthophotos (Ayman Habib, 2018), LiDAR, and image data integration for building modeling (Brenner, 2005), combining image and LiDAR data for automatic reconstruction of railroad centerline (Beger et al., 2011), and fusion of image and LiDAR point clouds for the derivation of Digital Surface Model (DSM) (Mandlburger et al., 2017).

(Toschi et al., 2021) has formulated a process based on aggregating the features and evaluating all 3D points sensor-specific and pointwise. Their integration approach has proven to work well with georeferenced point clouds without any flight trajectories, but it has some limitations with point density variation, misalignment within a point cloud, or point clouds acquired from different platforms. Acquisition of data from different UAS or terrestrial platforms would lead to point clouds with diverse quality and requires the selection of the most suitable quality features (Toschi et al., 2021).

A handful of research has been published on coregistration of image and LiDAR data but mostly are not simultaneously taking flight trajectory, the mounting calibration parameters and sensor parameters for LiDAR strip adjustment, and aerial triangulation. Most of the studies mainly aim at independent LiDAR block adjustment and coregistration of image data. An approach for LiDAR and image data coregistration was formulated based on combined information from LiDAR and imagery, with a statistical relationship between aerial images, LiDAR point cloud, and LiDAR intensity data (Parmehr et al., 2014). As per the integration framework by (Abayowa et al., 2015), the Iterative Closest Algorithm (ICP) was implemented to optimize the discrepancies between the Digital Surface Models (DSMs) obtained from LiDAR and image data. This approach was based on relative orientation by matching invariant and salient features in DSMs from LiDAR and imagery point clouds (Philipp Glira, 2018).

The adjustments of the LiDAR strips (Strip Adjustment, SA) and the Bundle Block Adjustment (BBA) for image rays with the same GNSS/INS trajectory have also led to an acceptable coregistration of the multi-sensor datasets. The Ground Control Points (GCPs) enable the refinement of the internal camera parameters, boresight calibration, and image orientations. The method of integrating point clouds from LiDAR with the camera images point cloud on the criterion of bias detection after adjustments had been a compelling method with the optimal need of GCPs collection for BBA (Toschi et al., 2018). The similar geometric features ( points, surfaces, and edges) create a transformation between different LiDAR reference frames and camera coordinate systems (A Habib et al., 2005; Peng et al., 2019).

(Yang & Chen, 2015) presented a sophisticated approach to integrating the image sequences and LiDAR data from a UAV, minimizing the discrepancies between two-point clouds. The approach was based on matching building outlines without any rigorous modeling of the measurements. In this approach, only a rigid body transformation was applied to match the images and LiDAR block, resulting in a moderate georeferencing accuracy.

The GNSS/INS-assisted LIDAR integration approach by (T. Zhou et al., 2021) initiates with the point cloud generation with point positioning equation, and LiDAR /GNSS assisted SfM followed by iterative identification of correspondences from both point clouds and integrated bundle adjustment. SIFT algorithm-based tie points are also established in this process to derive the sparse image point cloud after refining system calibration parameters from bundle adjustment. It also considers the planar constraint to the seed point to identify the corresponding patches from LiDAR data. Figure 2.3 illustrates the discrepancies associated with the point clouds from UAV-based LiDAR and camera data.

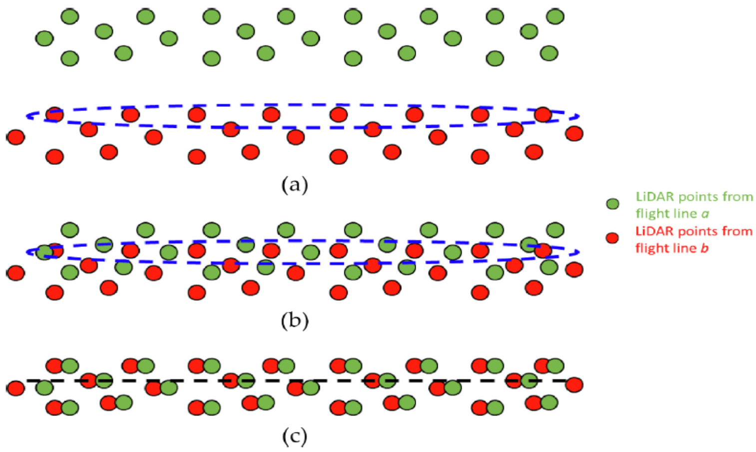


Figure 2.3: Alignment of two points a) two LiDAR point clouds with Z-discrepancy b) with a minimal 3D point to 3D point distance c) planar patch to planar patch discrepancy. Example is taken from (T. Zhou et al., 2021)

Another target-based image and LiDAR data integration approach was conducted by (Pentek et al., 2020), employing LiDAR strip adjustment (LSA) in the initial step, followed by using LiDAR point cloud from the initial step as a reference for the camera system calibration. 3D coordinates were estimated with the intersection between light rays from images and LiDAR points, minimizing the distance between these correspondences for every corresponding pair of image points from image matching. However, this integration approach did not consider the probable errors in the trajectory of data acquisition.

The hybrid adjustment approaches consider the simultaneous adjustment of both LiDAR and camera datasets. A unified process inclusive of the strip adjustment and bundle block adjustment was found to be more robust and efficient than the existing multi-sensor data integration approaches. (P Glira et al., 2019) framed a method for hybrid orientation with a rigorous and iterative determination of the correspondences between the image tie points and LiDAR points. However, this hybrid adjustment method optimizes the multi-sensor block stability and integrates the sensors with the possible inclusion of the UAS trajectory and ground truth data. The data-driven integration approach by (P Glira et al., 2019; Pentek et al., 2020) deals initially with LiDAR calibration followed by the camera calibration from the initial LiDAR point cloud product, i.e., using refined calibration from the one sensor as standard to calibrate the second sensor. Thus, there could be possible residual errors in the initial calibration, which could compromise the calibration quality of the second sensor with even more errors.

Figure 2.4 shows the point cloud from aerial LiDAR, aerial photogrammetry, and the integrated point cloud from LiDAR and photogrammetry. The integrated point cloud can have discrepancies or displacements due to different sensor characteristics and synchronization issues.

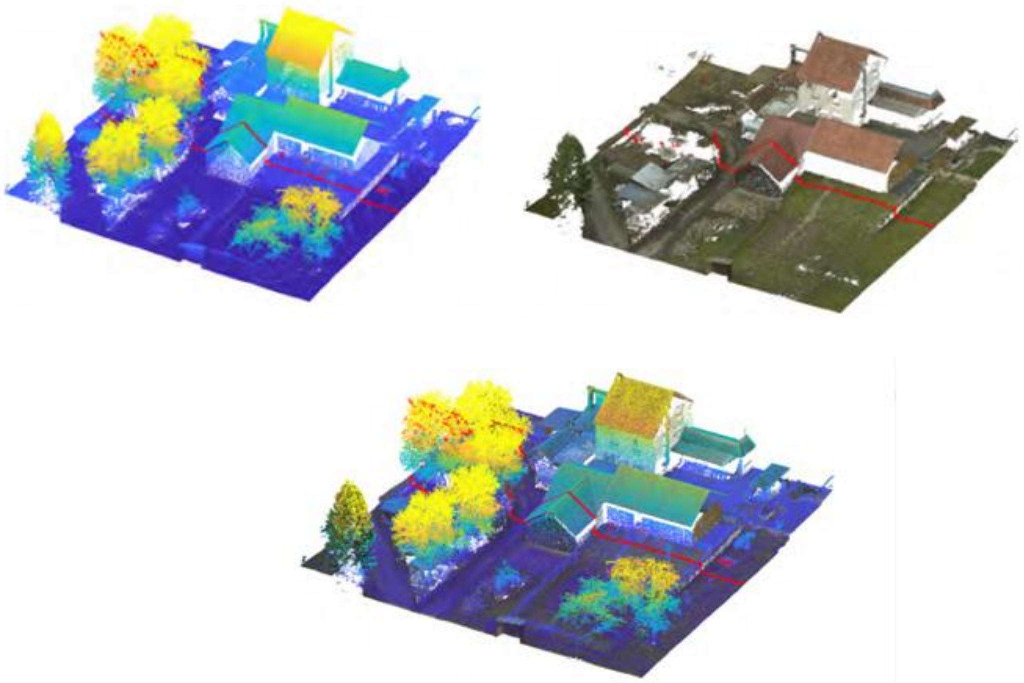

Figure 2.4: point cloud from LiDAR (top-left), point cloud from aerial imagery (top-right), and Integrated point cloud (bottom). Example is taken from (Philipp Glira, 2018)

In recent research, (N. Haala et al., 2020) have also developed an approach for generating ultra-high accurate LiDAR point clouds from UAVs by combining image measurements from block adjustments and trajectory corrections at the different photogrammetric processing steps. In this hybrid orientation approach, flight trajectory improved during LiDAR strip adjustment, followed by adding observations from the photogrammetry in the hybrid adjustment (N. Haala et al., 2020). The accuracies with this approach were achieved to the range of Ground Sampling Distance (GSD) of the imagery used. This approach was aimed to enhance the accuracy of LiDAR strips with the use of imagery.
In another state-of-the-art research by (Norbert Haala et al., 2022), the hybrid georeferencing of UAV-based LiDAR and camera images was implemented using image space tie points, checkerboard targets, and LiDAR control planes as additional inputs to improvise the accuracy of the adjustment. This research was motivated by monitoring the subsidence and with this approach. The achieved accuracy in this approach was in the range of millimeters with the use of additional observations in the adjustment.

## 2.5. What did we do differently in our hybrid adjustment approach?

The hybrid adjustment in our research is motivated to minimize the discrepancies between the point clouds derived from UAS-based camera images and LiDAR data. It also includes the constraints on several parameters like the roughness of the surfaces and threshold angle between normals of the surfaces, which affect the overall performance of the hybrid adjustment. A subset of corresponding points was selected with a uniform sampling technique instead of using all the points from LiDAR and image datasets to make the hybrid adjustment computationally efficient.
Most of the research works which have implemented the hybrid adjustment focus on the computation of DSM-based relative height differences for quality checks. In our workflow, we have also considered the computation and comparison of 3D cloud-to-cloud distances before and after hybrid adjustment as a primary quality check of the results. The 3D distances have also been investigated at the surface level for all the three datasets used in this research. As a secondary quality check, DSM-based relative height differences are also computed to cross-check the results from the primary quality check.

## 2.6. Research work (s) related to hybrid adjustment

The connected graph in Figure 2.5 shows the research related to the hybrid adjustment of UAS-based LiDAR and image data. The interactive graph and the detailed information can be found via this [link](). We expect this interactive graph to help the interested readers explore the related literature for further investigation.

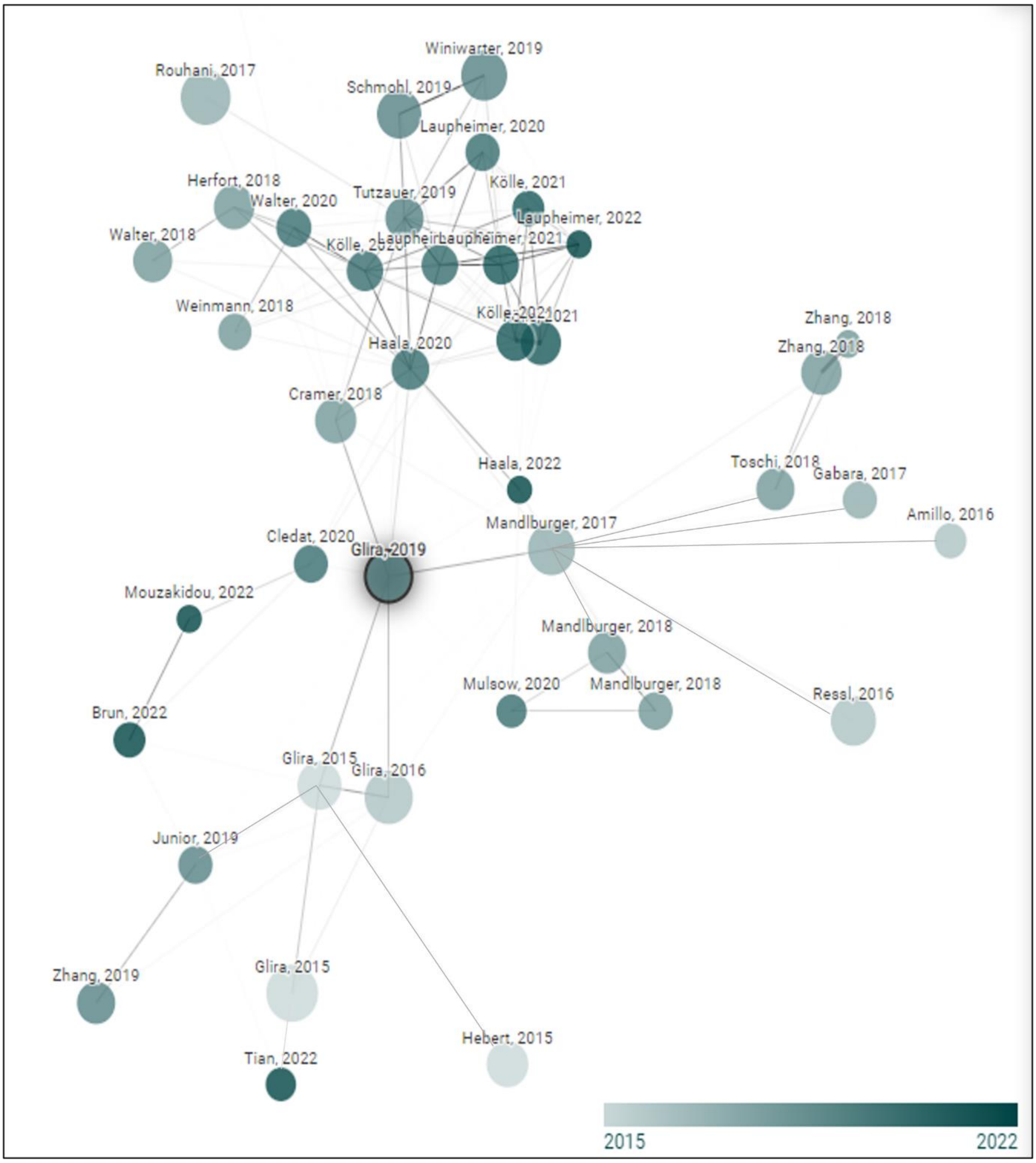


Figure 2.5: Graph showing the research works related to hybrid adjustment of multi-sensor datasets (Connected Papers, 2022)

# 3. STUDY AREA AND DATASET ACQUISITION SYSTEMS

This chapter describes the details of the study area and dataset used for this M.Sc. research work. It includes the dataset acquisition system, camera sensor, and LiDAR scanner used for the data acquisition phase. This section also gives insights into the software components and programming language used to implement the hybrid adjustment approach.

## 3.1. Study Area

The datasets were collected over a municipality in the south of Sardinia, an island located in Italy in the Mediterranean sea. Three datasets (dataset_A, dataset_B, and dataset_C) were acquired on 23rd April 2021 during planned flights over the study area. The study area comprises features like buildings, bare land, roads, and vegetation surfaces. The ground coverage of dataset_A, dataset_B, and dataset_C is 0.214 km$^2$., 0.221 km$^2$, and 0.148 km$^2$, respectively. Figure 3.1 shows the location of the study area under consideration for this research. Figure 3.2,Figure 3.3, and Figure 3.4 show the orthophoto and extent of dataset_A, dataset_B, and dataset_C, respectively.

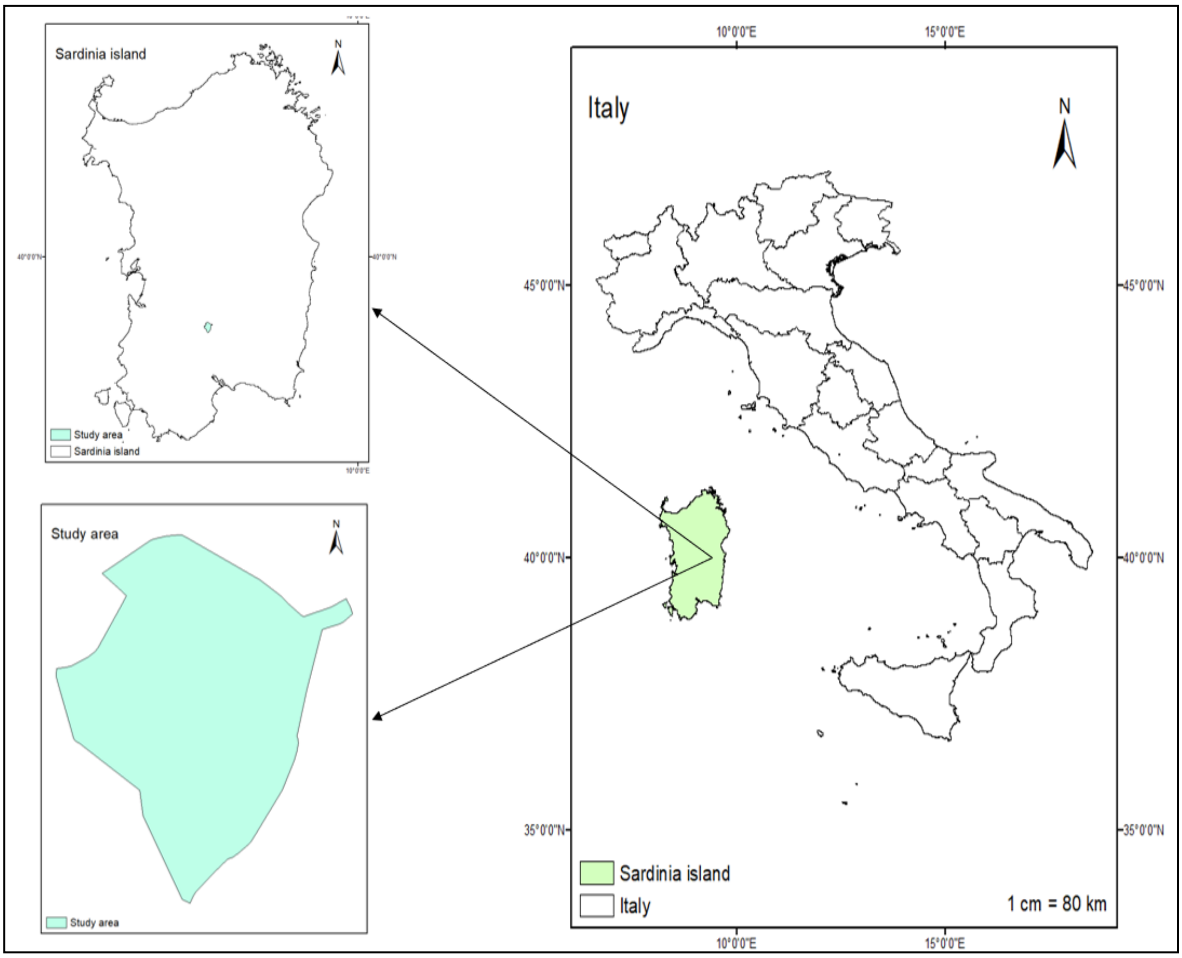


Figure 3.1: Location map of the study area

Extent:

min x y z: 498180.996 4378755.808 105.437
max x y z: 498814.715 4379367.773 163.254

Figure 3.2: orthophoto and extent of dataset_A

Extent:

min x y z: 498161.390 4379072.824 104.421
max x y z: 498818.763 4379662.166 163.658

Figure 3.3: orthophoto and extent of dataset_B

Extent:

min x y z: 497917.496 4379354.026 100.352
max x y z: 498448.983 4379803.953 151.579

Figure 3.4: orthophoto and extent of dataset_C

### 3.2. Data acquisition systems

For this research work, the dataset was acquired by (Alto-drones, 2021) with a UAS-based camera and LiDAR sensors. A custom-made hybrid UAS system with camera and LiDAR sensors mounted on it was flown over the study area on 23rd April 2021 for the data acquisition at a flight height of 98.6 m, 88 m, and 86.6. m for dataset_A, dataset_B, and dataset_C, respectively. SONY ILCE-7RM3 camera with a resolution of 7952*5304 pixels, a pixel size of 4.5 micrometers, and a focal length of 21mm was used to acquire camera images (SONY, 2022). For the laser scanning data acquisition, a RIEGL miniVUX-3UAV scanner was used, with a scanning rate of up to 100 scans per sec and up to 360 degrees of field of view (RIEGL, 2022). The hybrid UAS-system mounted with a camera and LiDAR sensor is shown in Figure 3.5 andFigure 3.6. The camera and LiDAR dataset characteristics are summarized in Table 3.1 and Table 3.2, respectively

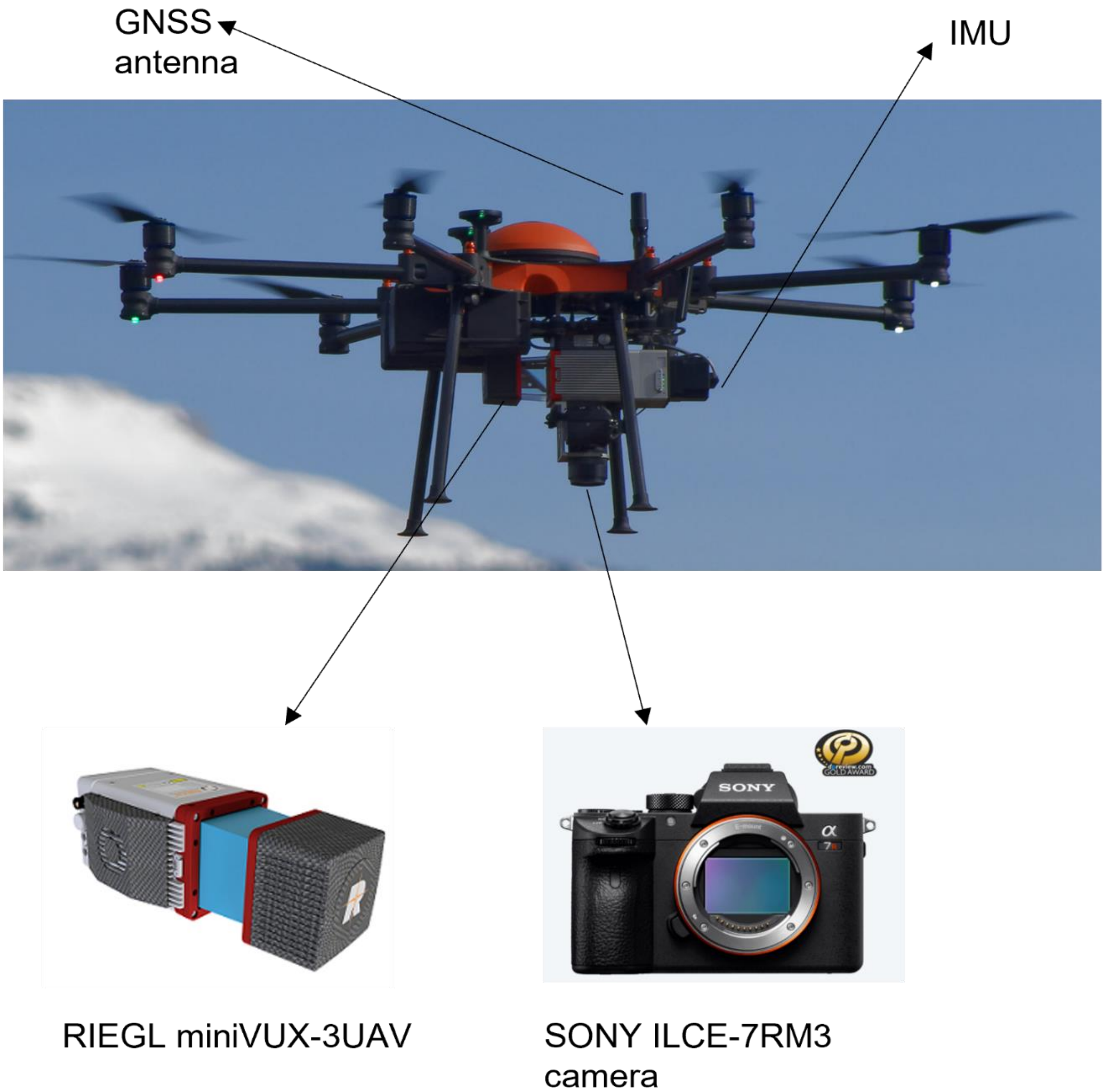


Figure 3.5: Dataset acquisition systems (Alto-drones, 2021; RIEGL, 2022; SONY, 2022)

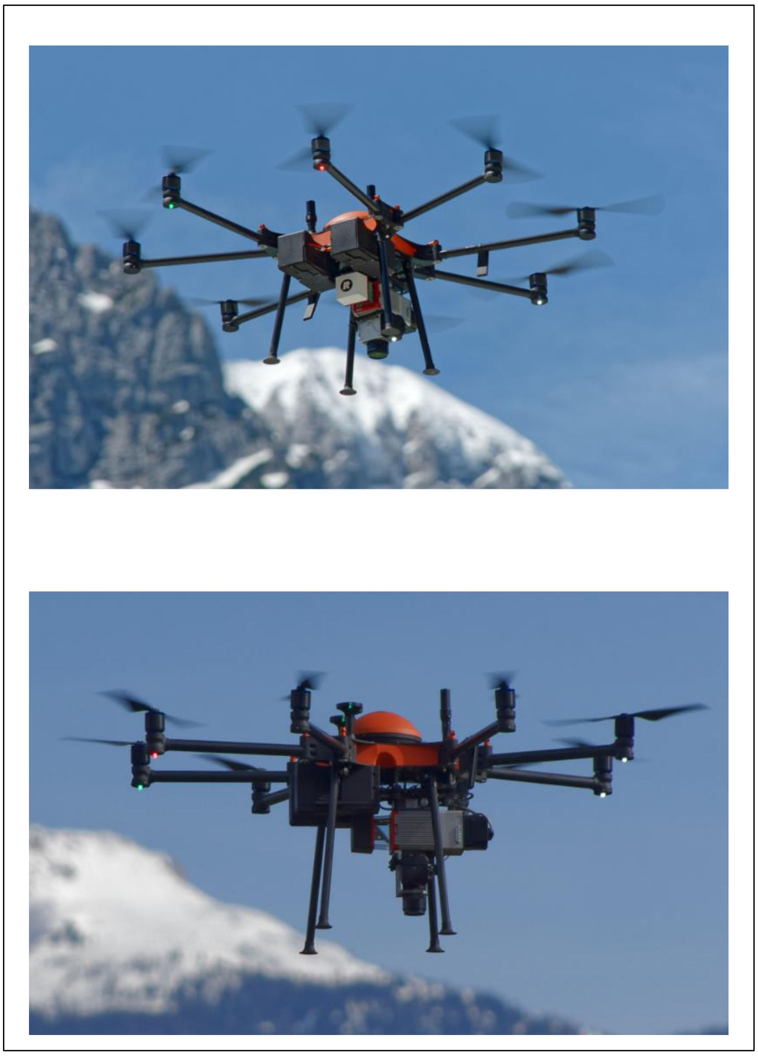

Figure 3.6: Hybrid UAS-system with LiDAR and camera sensors used in data acquisition

Table 3.1: Characteristics of camera data

| Characteristics | Information/Value |
|---|---|
| Camera type | SONY ILCE-7RM3 frame camera |
| Pixel size | 4.5 µm |
| Focal length | 21 mm |
| Image resolution | 7952 × 5304 pixels |
| Average Ground Sampling Distance (GSD) | 1.85 cm/pixel |

Table 3.2: Characteristics of LiDAR data

| Characteristics | Information/Value |
|---|---|
| Scanner type | RIEGL miniVUX-3UAV |
| Scan frequency | 5 milli-seconds, 200 Hz |
| Average point density | 51.39 points per m2 |
| Average point spacing | 0.14 m |

### 3.3. Dataset description

During the UAS flights, datasets from camera and LiDAR sensors were collected simultaneously. Image exposure stations were recorded with integrated GNSS/IMU systems at an interval of 5 milliseconds (frequency = 200 Hz) for all the camera images acquired with the camera. The description of the datasets used in the research is summarized in Table 3.3.

Table 3.3: Description of datasets used in the research

| Data type | Source | Description (dataset_A) | Description (dataset_B) | Description (dataset_C) |
|---|---|---|---|---|
| Raw LiDAR measurements | RiEGL scanner | 27 .rdbx files | 28 .rdbx files | 26 .rdbx files |
| Camera data | Sony frame camera | 277 camera images | 328 camera images | 224 camera images |
| Initial UAS trajectory | GNSS/IMU | Trajectory file (.txt) | Trajectory file (.txt) | Trajectory file (.txt) |

### 3.4. Software tools and programming language used

Agisoft Metashape Professional software was used to pre-process camera images with initial orientation parameters to generate image point observations for the hybrid adjustment. The StripAdjust module from OPALS modular program (Pfeifer et al., 2014) was used for the hybrid adjustment approach with optimal parameters and weights for the UAS datasets. Hybrid Adjustment process and Quality Control (QC) of adjustment was implemented in OPALS command shell with python environment. The misalignment between camera and LiDAR datasets before and after the hybrid adjustment implementation was analyzed in the CloudCompare (CloudCompare, 2021) software. Pix4DMapper software was used for dense point cloud generation from camera images. The summary of the software and tools used in this research work is presented in Table 3.4.

Table 3.4: Software/ programming tools used in the research

| S. No. | Software/package/programming language | Function |
|---|---|---|
| 1 | Agisoft Metashape Professional (64-bit) | Initial processing of camera images to generate inputs for hybrid adjustment |
| 2 | OPALS package | Implementation of the hybrid adjustment |
| 3 | Python | To access Opals package for hybrid adjustment |
| 4 | MATLAB runtime | To support Opals package in hybrid adjustment |
| 5 | Pix4DMapper | Post-processing of the images after the hybrid adjustment |
| 6 | CloudCompare | For the quality control of results and visualization of point clouds |
| 7 | ArcMap 10.8.2 | Creation of the study area map |
| 8 | Microsoft Office | Thesis writing, chart creation, and thesis presentation |
| 9 | Mendeley Desktop | Referencing in the thesis document |

# 4. CONCEPTUAL AND MATHEMATICAL FRAMEWORK

This section describes the basic conceptual and mathematical foundation which has been used in the hybrid adjustment process in this M.Sc. research work. This section starts with the first step in hybrid adjustment, implementing the modified ICP algorithm to establish different types of correspondences between the datasets, mathematical models, and equations used in the hybrid adjustment process.

## 4.1. Implementation of modified ICP algorithm

For the hybrid adjustment process implemented in this research work, the first elementary framework is the ICP algorithm (Besl & McKay, 1992; Chen & Medioni, 1991; Philipp Glira et al., 2015). Further modifications and extensions made to the basic version of the ICP algorithm have been used for the hybrid adjustment process. This hybrid adjustment process of UAS-based LiDAR and camera data is fundamentally based on the three aspects of the ICP algorithm

- Establishment of correspondences between point clouds iteratively
- Using the closet point as correspondence (corresponding point)
- Establishment of correspondences as point-to-point in two datasets

LiDAR data collected with UAS have an ample amount of overlapping area w.r.t. corresponding strip, and the mounting calibration of the laser scanners can be fetched from the raw LiDAR measurements. The fundamental framework of the ICP algorithm is as follows:

1. Selection: Subset of the points from the overlap area of the fixed-point cloud
2. Matching: Search and match for the corresponding point of a selected subset of points in the movable point cloud
3. Rejection: Outliers/false correspondences are rejected
4. Minimization: Estimation of transformation parameters for the movable point cloud by minimizing the distances between corresponding point subsets
5. Transformation: Movable point cloud transformation with estimated parameters
6. Iteration: If a suitable convergence criterion is not met, the iteration starts again from the selection step until the convergence criterion is met.

Let $p_{[n]}$ and $q_{[n]}$ be two-point clouds with the same number of points N. Initially, the two-point clouds are roughly aligned with some misalignment, i.e., the discrepancies within the overlap area of two-point clouds are smaller as compared to their object size. The point cloud $p_{[n]}$ is defined as the fixed point cloud in the object space. The ICP algorithm finds a rigid transformation T for the movable point clouds $q_{[n]}$ to minimize the discrepancies in two-point clouds. The transformation T is defined by

$$T(q_{[n]}) = Rq_{[n]} + t \tag{4.1}$$

where t denotes a 3 × 1 translation vector, and R denotes a 3 × 3 orthogonal rotational matrix.
The correspondences between the two points are established by pairing each point in $p_{[i]}$ to the nearest neighbor in $q_{[i]}$ . The discrepancies between these corresponding points can be described by different error metrics. The Euclidean distance (point-to-point distance) is used as an error metric, which is defined by:

$$d_{[p]} = |\, p_{[i]} - q_{[i]}| \tag{4.2}$$

where $d_{[p]}$ is the euclidean distance between two corresponding points.

The main objective of the optimization with the ICP algorithm is to minimize the squared point-to-point distance. One closest solution to this objective was proposed by (Horn, 1987), which did not require any iterations and initial parameter values. This solution was used in the adjustment process to directly estimate the rotation matrix R and translation vector t for the movable point cloud from our set of correspondences.

Initially, the centroids of both point clouds ($p_C, q_C$) has to be computed. The reduced coordinates are given by

$$p^c_{[i]} = p_{[i]} - p_C \quad (4.3)$$

$$q^c_{[i]} = q_{[i]} - q_C \quad (4.4)$$

where the points are ordered in both point clouds according to the previously established correspondences. The covariance matrix can be computed by

$$S = PQ^T \quad (4.5)$$

where P and Q are 3-by-N matrices with $p^c_{[i]}$and $q^c_{[i]}$ as columns of the matrices, respectively.

The major limitation of the basic ICP algorithm was that the two-point clouds need to have the same number of points and should be fully overlapping. The modified version of the ICP algorithm includes selecting points, weighing the correspondences, and error metric for measuring the distance between the corresponding points.

## 4.2. Hybrid adjustment approach

The hybrid adjustment approach simultaneously optimizes the relative and absolute orientation of the LiDAR strips (STR) and the camera images (IMG), with the possibility of using Ground Control Points (GCPs) and Control Point Clouds (CPCs). In this M.Sc. research, no GCPs or CPCs have been used; only raw measurements from scanner and camera data have been used for the hybrid adjustment.

The methodological basis for the hybrid adjustment (Philipp Glira, 2018; Pfeifer et al., 2014) adopted in this research has been formed by the correspondences framework of a basic version of the ICP algorithm discussed earlier, with the several extensions:

- The basic ICP algorithm is restricted to two-point clouds, whereas the hybrid adjustment can be used for any number of point clouds. These point clouds can be LiDAR strips, image tie point observations, or the ground truth data in the form of Ground Control Points or Control Point Clouds
- The alignment of the point clouds is optimized simultaneously in a single least square adjustment as opposed to a sequential alignment of overlapping point cloud pairs
- Instead of using every point from the camera and LiDAR datasets as correspondence, the query points selected with a uniform sampling technique were used in the hybrid adjustment.
- The point-to-plane distance is used as an error metric instead of point-to-point distance. Consequently, the corresponding points do not need to be identical in object space, but they should only belong to the same plane.
- Several correspondences rejection criteria were used to detect and eliminate the false correspondences or outliers, followed by a robust adjustment method for the removal of outliers.
- The simultaneous integration of bundle adjustment of aerial images, i.e., aerial triangulation into the ICP framework, allows simultaneous orientation and calibration of LiDAR point clouds and aerial images. The camera images are connected to LiDAR strips by images tie points (sparse feature point cloud) and the common flight trajectory
- The calibration parameters of the camera (focal length, principal point, and distortion parameters) and LiDAR scanner (systematic range and angle measurements) can also be adjusted and estimated in the hybrid adjustment process

- Two trajectory correction models were used to correct the systematic errors of the flight trajectory,
  i) Bias Trajectory Correction Model
  ii) Linear Trajectory Correction Model
- The image and LiDAR observations are also weighted in the hybrid adjustment, which was not considered in the standard version of the ICP algorithm

## 4.3. Mathematical foundation of the hybrid adjustment

This sub-section describes the equations to relate the measurements from the camera, LiDAR sensors, GNSS, and INS to the observed object points on the ground. These equations were used in the hybrid adjustment to establish the correspondences and formulate the adjustment's observations.
The relation between observations from the LiDAR sensor and ground measurements is expressed by the direct georeferencing equations. In the case of camera images, the relation between camera measurements and ground observations is given by the direct georeferencing equation and the collinearity equations. The GNSS/INS flight trajectory is shared by camera images and LiDAR strips through the respective direct georeferencing equations. The parameter model connecting different observations in the hybrid adjustment is shown in Figure 4.1.

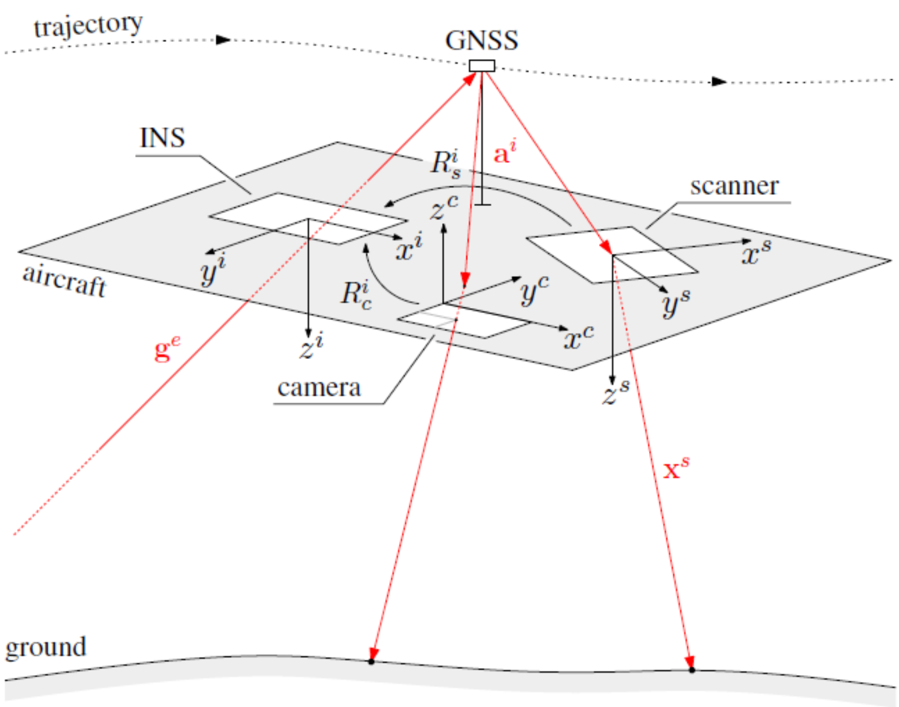


Figure 4.1: Parameter model used in the hybrid adjustment (Philipp Glira, 2018)

In Figure 4.1,
- $x^s, y^s, z^s$ are the coordinate of the laser point
- $x^c, y^c, z^c$ are the image point coordinate in image space
- $g^e$ vector describing the position of GNSS
- $a^i$ is the positional offset between the GNSS antenna and projection center of the camera
- $R_s^i$ is the rotation from the scanner-coordinate system to the INS-coordinate system
- $R_c^i$is the rotation from the camera coordinate system to the INS-coordinate system

### 4.3.1. Direct georeferencing of UAS-based LiDAR strips

The direct georeferencing equation generates georeferenced point clouds from the raw LiDAR data strips. The following data inputs are required for the direct georeferencing equation (Hebel & Stilla, 2012; Jan Skaloud & Lichti, 2006) :

- Mounting calibration parameters
- Polar measurements of the scanner
- Flight trajectory of the aircraft

The point coordinates of an object point [o] measured by a LiDAR scanner [*l*] at a time t are given by (Philipp Glira, 2018):

$$x^e_{[o]} = g^e(t) + R^e_{[n]}(\mathrm{t})\, R^n_i\,(t)\;(\;a^i_{[l]} + R^i_{s[l]}\mathrm{x}^s_{[o]}\,) \tag{4.6}$$

The superscript of the vector represents the coordinate system in which the vector is defined. Four coordinate systems can be observed in equation 4.6, where "s" represents the scanner coordinate system, "i" for INS/body coordinate system, "n" for the navigation coordinate system, and e stands for ECEF coordinate system (Bäumker & Heimes, 2002). This research work implemented the hybrid adjustment entirely in the ECEF (Earth Centered Earth Fixed) coordinate system.

- $\mathrm{x}^s_{[o]}$ is a 3 × 1 vector with coordinates of laser point [o] in the e-system. These coordinates can be expressed as a function of the range $\rho_{[o]}$ and two angles $\alpha_{[o]}$ and $\beta_{[o]}$ by:
- 

$$\mathrm{x}^s_{[o]}\;(t) = \;\mathrm{x}^s_{[o]}\;(\,\rho_{[o]}, \alpha_{[o]}, \beta_{[o]} \tag{4.7}$$

- $R^i_{s[l]}$ is a 3 × 3 rotation matrix describing the rotation from s-system to i-system, denoted as boresight alignment and parametrized through 3 Euler angles $(\,\alpha_1, \alpha_2\,, \alpha_3)$:

$$R^i_{s[l]} = R^i_{s[l]}(\,\alpha_{1[l]}, \alpha_{2[l]}\,, \alpha_{3[l]}) \tag{4.8}$$

- $a^i_{[l]}$ is a 3 × 1 vector describing the positional offset between GNSS antenna and the origin of e-system, denoted as lever arm:

$$a^i_{[l]} = \left[\,a^i_{x[l]}\;\; a^i_{y[l]}\;\; a^i_{z[l]}\right]^T \tag{4.9}$$

- $R^n_{[i]}(t)$ is a 3 × 3 rotation matrix describing rotation from the i-system to n-system as the first part of trajectory data which can be estimated from GNSS/INS measurements and parametrized through three Euler angles roll $\phi$ , pitch $\theta,$ and yaw $\psi$ :

$$R^n_{[i]}(t) = R^n_{[i]}(\,(\phi(t), \theta(t), \psi(t) \tag{4.10}$$

- $g^e(t)$ is a 3 × 1 vector describing the position of GNSS antenna in e-system as the second part of trajectory data:

$$g^e(t) = [\,g^e_x(t)\;\; g^e_y(t)\;\;\; g^e_z(t)\,] \tag{4.11}$$

- $R^e_{[n]}(t)$ is a 3 × 3 rotation matrix describing the rotation from n-system to e-system as a function of the longitude $\lambda$ and latitude $\varphi$ corresponding to the actual value of $g^e(t)$:

$$R^e_{[n]}(t) = \;R^e_{[n]}(\lambda\,(t), \varphi(t) \tag{4.12}$$

The six mounting calibration parameters are represented in equation (4.6) by the rotation matrix $R^i_{s[l]}$ are defined by three misalignment angles $(\,\alpha_1, \alpha_2\,, \alpha_3)$ and three lever arm components. Usually, mounting calibration parameters are already known for the sensor platform. However, these parameter values can be inaccurate and can contribute to incorrect misalignment causing large point displacements because the effect of angular errors is directly proportional to object distance. Many strip adjustment approaches have focused on the estimation of boresight $R^{i}_{s[l]}$ without the consideration of mounting calibration parameters. The systematic errors of LIDAR scanner measurements $\mathrm{x}^{s}_{[o]}$ are compensated by the scanner calibration parameters. The scanner calibration parameters for the systematic errors of range and angle measurements in LiDAR observations.

#### 4.3.2. Direct georeferencing of UAS-based camera images

The exterior orientation of an image, i.e., image pose, is the position of the projection center of the camera (coordinates X, Y, and Z) and the rotation of the image w.r.t object coordinate system. The exterior orientation of an image is usually described in terms of a rotation matrix R which can be derived from:

- Flight trajectory of UAS system
- Mounting calibration parameters of the camera

The images for which the exposure time “t” is known are termed “Coupled” images as their exterior orientation is tied to a flight trajectory. The exterior orientation parameters of these images can be formulated through a direct georeferencing equation as a function of flight trajectory and camera mounting calibration parameters. The projection center and rotation matrix of coupled images for $i^{th}$ image at time t is given by (Philipp Glira, 2018):

$$x^{e}_{0[i]}(t) = g^{e}\ (t) + R^{e}_{n}(t)R^{n}_{i}(t)a^{i}_{[c]} \tag{4.13}$$

$$R^{e}_{c[i]}(t) = R^{e}_{n}(t)R^{n}_{i}(t)R^{i}_{c[c]} \tag{4.14}$$

where

- Subscript $c$ represents the camera coordinate system
- $x^{e}_{0[i]}(t)$ is the $3 \times 1$ vector with the image’s projection center coordinates in e-system

$$x^{e}_{0[i]}(t) = \left[\, X^{e}_{0[i]}(t) \quad Y^{e}_{0[i]}(t) \quad Z^{e}_{0[i]}(t)\,\right]^{T} \tag{4.15}$$

- $R^{e}_{c[i]}$ is a $3 \times 3$ rotation matrix describing the three-dimensional rotation/altitude of the camera w.r.t. e-system. This is parametrized through three Euler angles omega $\omega_{[i]}$, phi $\varphi_{[i]}$ and kappa $\kappa_{[i]}$:

$$R^{e}_{c[i]} \ = \ R^{e}_{c[i]}\left(\,\omega_{[i]}, \varphi_{[i]}\,, \kappa_{[i]}\right) \tag{4.16}$$

- $a^{i}_{[c]}$ is a $3 \times 3$ vector describing the positional offset between GNSS antenna and projection center of the camera, denoted as lever arm:

$$a^{i}_{[c]} = [\ a^{i}_{x[c]} \quad a^{i}_{y[c]} \quad a^{i}_{z[c]}]^{T} \tag{4.17}$$

- $R^{i}_{c[c]}$ is a $3 \times 3$ rotation matrix describing camera rotations (c-system) to the INS system (i-system), denoted as boresight misalignment, and is parametrized through three Euler angles $\beta_1, \beta_2, \beta_3$ :

$$R^{i}_{c[c]}= R^{i}_{c[c]}(\,\beta_{1[c]},\ \beta_{2[c]}, \beta_{3[c]}) \tag{4.18}$$

Loose images are those for which relation to flight trajectory is not known. In the case of loose images, where timestamps "t" of the camera images are unknown, or GNSS/INS trajectory is not available for the dataset, the direct georeferencing equation cannot be used. In the case of hybrid adjustment with loose images, the positional $[X^e_{0[i]}(t), Y^e_{0[i]}(t), Z^e_{0[i]}(t)]$ and rotational elements $(\omega_{[i]}, \varphi_{[i]}, \kappa_{[i]})$ of the exterior elements of the images are directly estimated by the adjustment.

### 4.3.3. Collinearity equations

The collinearity equations correlate 2D image coordinates with 3D object coordinates of a single point in object space. For an object point [o] observed in an image [i] taken by a camera [c], collinearity equations are given by:

$$\bar{x}^c_{[i][o]} = x^c_{o[c]} - c^c_{[c]} \frac{[\,r_{11}(X^e_{[o]} - X^e_{0[i]}) + r_{21}(Y^e_{[o]} - Y^e_{0[i]}) + r_{31}(Z^e_{[o]} - Z^e_{0[i]})}{[\,r_{13}(X^e_{[o]} - X^e_{0[i]}) + r_{23}(Y^e_{[o]} - Y^e_{0[i]}) + r_{33}(Z^e_{[o]} - Z^e_{0[i]})} \tag{4.19}$$

$$\bar{y}^c_{[i][o]} = y^c_{o[c]} - c^c_{[c]} \frac{[\,r_{11}(X^e_{[o]} - X^e_{0[i]}) + r_{21}(Y^e_{[o]} - Y^e_{0[i]}) + r_{31}(Z^e_{[o]} - Z^e_{0[i]})}{[\,r_{13}(X^e_{[o]} - X^e_{0[i]}) + r_{23}(Y^e_{[o]} - Y^e_{0[i]}) + r_{33}(Z^e_{[o]} - Z^e_{0[i]})} \tag{4.20}$$

where

- $\bar{x}^c_{[i][o]}$, $\bar{y}^c_{[i][o]}$ are the undistorted image coordinates
- $x^c_{o[c]}$, $y^c_{o[c]}$ are coordinates of principal points of the camera
- $c^c_{[c]}$ is the principal distance of the camera
- $X^e_{0[i]}$, $Y^e_{0[i]}$, $Z^e_{0[i]}$ are the coordinates of the projection center of the camera
- $r_{ij}$ are the elements of the rotation matrix $R^e_{c[i]}$ in equation 4.14
- $X^e_{[o]}$, $Y^e_{[o]}$, $Z^e_{[o]}$ are the coordinates of the object point [o]

The collinearity equation is valid for an ideal perspective camera only, and deviation from the ideal perspective is modeled by image distortion coefficients. The image distortion coefficients, together with projection center coordinates and the principal distance, form the camera calibration parameters. The camera calibration parameters are estimated in the bundle adjustment process to reconstruct the earth's surface accurately.

### 4.3.4. Trajectory correction parameters

The original trajectory of the UAS system establishes the basis for the direct georeferencing of UAS-based LiDAR strips and camera images. However, (Jan Skaloud et al., 2010) concluded that GNSS and INS trajectory measurements are strongly affected by external influences like flight maneuvers and satellite constellation. The accuracy in the measurements cannot be treated as constant w.r.t. time, leading to the time-dependent errors of the estimated trajectory, to be corrected by adjustment. The six trajectory elements of original position $[\,g^e_{x_0}(t), g^e_{y_0}(t), g^e_{z_0}(t)\,]$ and original orientation $[\,\phi_0(t), \theta_0(t), \gamma_0(t)]$ are corrected in the hybrid adjustment for each LiDAR strip /image by a correction function $\Delta(.)_{[s]}(t)$.
The simplest trajectory correction model is the Bias Trajectory Correction Model (BTCM), which corrects a bias (by 0-degree polynomials) for each of six trajectory elements, individually for each strip (Philipp Glira, 2018).

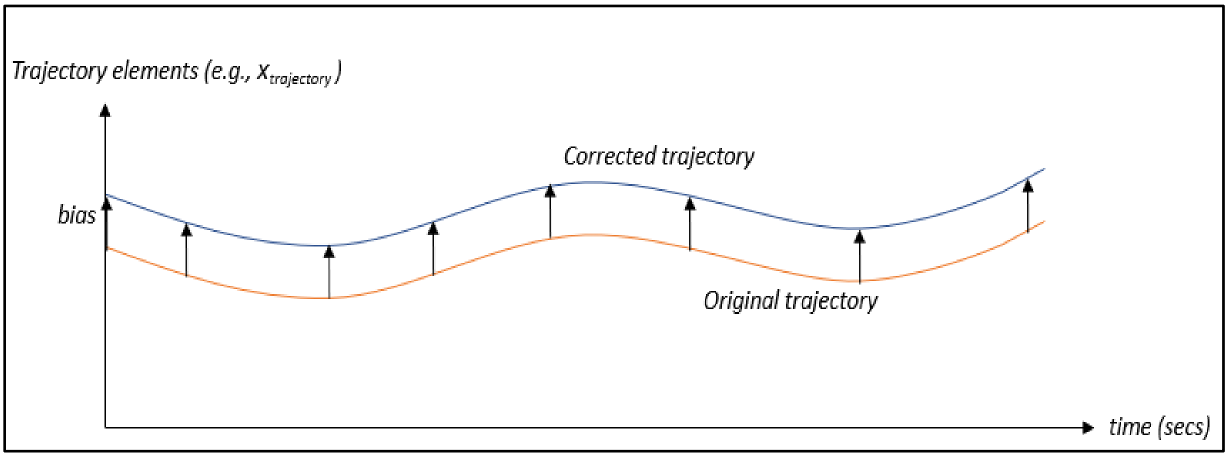


Figure 4.2: Bias trajectory correction model (BTCM)

The correction model for BTCM for a single strip [s]is given by :

$$\Delta\theta_{[s]} = a_{0[s]} \tag{4.21}$$

where correction coefficient $a_{0[s]}$ is estimated by the hybrid adjustment.

The second trajectory model is the Linear Trajectory correction model (LTCM), which was used in the hybrid adjustment. LTCM corrects the trajectory with a 1-degree polynomial.

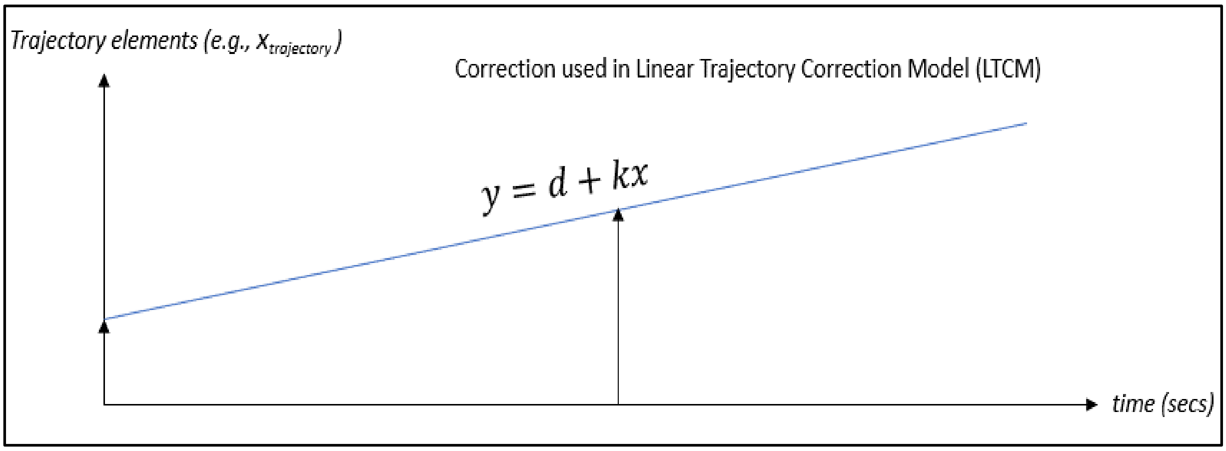


Figure 4.3: Linear Trajectory Correction Model (LTCM)

The correction model for LCTM for a single strip [s] is given by:

$$\Delta\theta_{[s]} = a_{0[s]} + \ a_{1[s]}(t - t_{s[s]}) \tag{4.22}$$

where

$t_{s[s]}$ is the starting time of the strip [s] and $t$ is the timestamp of the trajectory estimate. The correction coefficients $a_{0[s]}$ and $a_{1[s]}$ are estimated by the hybrid adjustment algorithm. The trajectory correction in LTCM follows a linear path given by the equation (4.23)

$$y = d + kx \tag{4.23}$$

where coefficients $d, k$ are estimated in the adjustment.

## 4.4. Correspondences between LiDAR and image data

The various types of correspondences have been used in the hybrid adjustment to simultaneously improve the georeferencing of LiDAR strips and camera images. In this work, the correspondences from LiDAR strips (STR) and camera images (IMG) were established and used in the hybrid adjustment process.

- STR: given by the scanner measurements, aircraft trajectory, and priors for mounting calibration
- IMG: given by either coupled images which are coupled to a trajectory by a timestamp and mounting calibration or images with prior known exterior orientation (loose images)

The three types of correspondences (IMG-IMG, STR-STR, and IMG-STR) have been used in the hybrid adjustment process to establish a link between LiDAR strips and camera images. The various correspondences define the observations used to estimate parameters in the hybrid adjustment process. This hybrid adjustment has considered three main steps to establish the correspondences in the object space: Selection, matching, and rejection of correspondences. This ensures the filtering of the suitable surfaces and points to be used in the hybrid adjustment.

### 4.4.1. Selection of the points for correspondences

The correspondences are selected on a point basis to use the highest possible resolution level of data in the hybrid adjustment. Another reason is that there are no restrictions on the object space. In the basic version of the ICP algorithm, every point is selected as correspondence, which is not feasible in the case of LiDAR strips, where

- a large number of strips have to be processed simultaneously
- a higher density of points in case of LiDAR strips

So, compared to all the available large number of points, only a comparatively smaller number of points can be selected within the overlap area of each strip pair. Since the accuracy of the selected subset of points significantly affects the adjustment accuracy, the selection of relevant points is essential for the adjustment process.
This hybrid adjustment approach has considered the more straightforward Uniform Sampling strategy to select correspondences within the overlap area of camera and LiDAR datasets. The main reason is to select the points uniformly in the object space. The uniform sampling selection strategy is applied to the correspondences established in the object space, namely STR-STR and IMG-STR.

**Uniform Sampling Technique**: This technique seeks to choose points in object space as evenly as possible, resulting in a homogeneous distribution of the selected points, with areas of equal area-weighted equally in the adjustment. On the other hand, if a normal direction is dominant, numerous duplicate locations with nearly parallel normal vectors are chosen, which have no major effect on parameter estimation. This option can be deleted by separating the overlap region into voxels and picking the point which is closest to each voxel center. As a result, a single voxel's edge length may be interpreted as the mean sampling distance along each coordinate direction. The uniform sampling approach uses the coordinates of the points rather than their normal vectors.
The quality of parameter estimation primarily depends on the selected subset of the points. If too many correspondences are established from featureless regions, the adjustment cannot converge due to a lack of constraints. In this hybrid adjustment approach, the selection of points is carried out with the uniform selection strategy, minimizes the uncertainty of estimated transformation parameters, and very few points (filtered out after selection strategies) are sufficient for the alignment of overlapping strips.

#### 4.4.2. Matching of the correspondences

After selecting query points, the correspondences are established with each point paired to the one point in the overlapping point cloud. The simplest strategy was given by (Besl & McKay, 1992) to match the selected points to their nearest neighbor points. This is an adequate choice for LiDAR and image data due to their compatible preliminary relative orientation and a higher point density of LiDAR strips. The k-d trees function can efficiently search the nearest neighbor points (closest point).

#### 4.4.3. Rejection of the correspondences

The purpose of this step is the rejection of the false correspondences (outliers) from the correspondences after the matching step, as they significantly affect the results of the adjustment and parameters estimation. The following correspondences rejection criteria can be applied are:

i) Rejection based on the reliability of the normal vectors of the corresponding points

For the point-to-plane error metric, the normal vectors of corresponding points are required, which can be estimated for each point using a principal component analysis of the covariance matrix of coordinates of the neighboring points (Shakarji, 1998). The neighborhood should be selected based on a fixed radius search, where the search radius should be chosen according to the point density and topography of the strips. The principal components of the covariance matrix are its eigen vectors, and the associated eigen values correspond to the variance in the direction of eigen vectors. The closest eigen vector ($\lambda_c$) is assumed as the least square estimate for the normal vector of the adjusting plane. The square root of $\lambda_c$ can be treated as a reliability measure for the normal vector. This value corresponds to the standard deviation of the selected points from an estimated plane and can be construed as a measure of the roughness of the adjusting plane.

$$\sigma_p = \sqrt{\lambda_c} \tag{4.24}$$

For the higher reliability of the normal vectors, corresponding points within rough areas should be rejected for the adjustment process.

ii) Rejection based on the angle between the normal vectors of corresponding points

This criterion rejects the correspondences with the differing plane orientations. For this, the angle between the normals of two corresponding points $p_{[i]}$and $q_{[i]}$is used.

$$\alpha = \arccos\left(n^T\, p_{[i]}.\, nq_{[i]}\right) \tag{4.25}$$

where

- $\alpha$ is the angle between the normal of two corresponding points
- $p_{[i]}$ and $q_{[i]}$ are normal of two corresponding points

To ensure two corresponding points belong to the same plane, the correspondences with $\alpha$ larger than 5° have been rejected in the hybrid adjustment.

iii) Rejection based on the distance between the corresponding points:

The distribution of a priori distances between corresponding points was analyzed. For the point-to-plane error metric, the signed distances $d_{[p]}$ are assumed to have a Gaussian distribution. The standard deviation of this normal distribution is given by:

$$\sigma_{mad} = 1.4826\ \times\ mad \tag{4.26}$$

$$mad = median\left(d_{[i]} - d\right) \tag{4.27}$$

where

- $\sigma_{mad}$ is the standard deviation of the gaussian distribution of signed point-to-plane distances
- $mad$ is the median of the absolute differences between corresponding points
- $d_{[i]}$ represents the signed distances in the point-to-plane error metric
- $d$ is the median of the point to plane distances.

The correspondences with distance outside the range of $d_{max} = d \pm 3\,\sigma_{mad}$ were rejected in the hybrid adjustment process.

### 4.4.4. Types of correspondences

The three types of correspondences are established in this research work: IMG-IMG, STR-STR, and IMG-STR. The correspondences STR-STR and IMG-STR have been established in the object space, whereas IMG-IMG correspondences in the image space.

i) IMG-IMG correspondences

The correspondences between Image pairs form the basis for the bundle block adjustment of the images for which the mathematical foundation is given by collinearity equations (4.18) and (4.19). Local feature matching algorithm Scale Invariant Feature Transform(SIFT) and its descriptor Histogram of Oriented Gradients (HOG) are used to establish correspondences between overlapping image pairs (IMG-IMG). The image tie points with unknown coordinates $( X^e[t], Y^e[t], Z^e[t])$ which are estimated by the adjustment. The objective of IMG-IMG correspondences is to minimize the weighted sum of squared residuals (reprojection errors).

ii) STR-STR correspondences

These correspondences are established within the overlap area of two overlapping LiDAR strips. The correspondences are established for each LiDAR strip pair by the selection, matching, and rejection steps mentioned in previous sections. Two points define a single correspondence from overlapping strips and their normal vectors estimated from neighboring points. A tangent plane is defined by a point and its normal vector, consequently a correspondence representing two homologous tangent planes in the object space. In the adjustment, the weighted sum of squared point-to-plane distances is minimized.

$$\Omega_{\mathrm{STR-STR}} = \operatorname{argmin} \left\{ \sum_{[i]=1}^{P} (w_{[i]} d_{[i]}^2 \right\} \tag{4.28}$$

where $w_{[i]}$ denotes the weight and $d_{[i]}$ represents the point-to-plane distance of $i^{th}$ correspondence defined by the points $p_{[i]}$ and $q_{[i]}$. The weights of the correspondences $w_{[i]}$ could be estimated in a mathematically rigorous way by propagating the errors of original measurements on point-to-plane distances $d_{[i]}$ , considering influencing factors like the precision of mounting calibration parameters and roughness of the surface. In order to avoid the need for these inputs of influencing factors, the precision of point-to-plane distances from the previously established correspondences has been estimated. Considering the correspondence "$i$" from a strip pair [k], then its weight is determined by equation 4.29.

$$w_{[i]} = \frac{1}{\sigma^2{}_{mad[k]}} \tag{4.29}$$

$$\sigma_{\,mad_{[k]}} = 1.4826 \times mad_{[k]} \tag{4.30}$$

where $mad$ is the median of absolute differences w.r.t. median of all point-to-plane distances belonging to the strip pair [k] and $\sigma_{mad_{[k]}}$ is the robust estimator for the standard deviation for the set of correspondences with possible false correspondences and outliers.

iii) IMG-STR correspondences

These correspondences are established within the overlap area of camera images and LiDAR strips. The specific data acquisition characteristics of both LiDAR and camera sensors should be considered while integrating LiDAR and image measurements. The surface reconstruction from the photogrammetry depends primarily on the sufficient texture variance, whereas LiDAR relies on the diffused backscattering of the emitted laser pulse. The only areas with the same view of the earth's surface from LiDAR and camera scanner should be considered for these types of correspondences. The IMG-STR correspondences are established as usual by the selection, matching, and rejection steps as for earlier correspondences.

The uniform sampling approach is used in the first stage to choose a subset of picture tie points (selection step). The correspondences are then formed by comparing the image tie points within the nearest neighbor in LiDAR point clouds in the matching step. Finally, possibly erroneous correspondences or outliers are excluded using the threshold criteria outlined previously in the rejection stage. The point-to-plane distances are formulated as:

$$d_{[i]} = \left(p_{[i]} - q_{[i]}\right)^T n_{[i]} \tag{4.31}$$

where

- $p_{[i]}$ represents the image tie points
- $q_{[i]}$ represents the points from the LiDAR strips
- $n_{[i]}$ is the normal vector in point $p_{[i]}$

## 4.5. Error metric

The hybrid adjustment aims to minimize the distance between the correspondences established in the earlier steps, i.e., minimization of error metric. The point-to-plane distances are the signed perpendicular distance of one point to the tangent plane of the other corresponding point (Chen & Medioni, 1992). The point-to-plane error metric has been chosen for the hybrid adjustment because of its better and faster convergence performance. The least-squares objective function of the point-to-plane error metric is:

$$\Omega_{\text{point-to-plane}} = \operatorname{argmin}\left\{\sum_{[i]=1}^{P} \omega_{[i]} d_{[i]}^2\right\} \tag{4.32}$$

where

- $\omega_i$ is the weight of the observations
- $d_i$ is the point to plane distances given by equation 4.31
- $p_i, q_i$ are corresponding points from $i^{th}$correspondence
- $n_i$ is a normal vector in the point $p_i$

All corresponding points do not need to be identical in object space for the point-to-plane error metric. The only requirement is that corresponding points lie on the same plane in object space (roof, road, or street). This error metric has a faster convergence speed because flat regions can slide along each other without increasing the objective function value in equation 4.32.

# 5. METHODOLOGY WORKFLOW

This chapter describes the step-by-step workflow of the hybrid adjustment involved in this research work. The hybrid adjustment workflow starts with pre-processing the camera and LiDAR data, followed by the hybrid adjustment of the LiDAR strips with loose and coupled images. The last section of this chapter describes the quality checks used for the results of the hybrid adjustment. Figure 5.7 represents the complete methodology flowchart from the preprocessing of the LiDAR and camera datasets followed by the hybrid adjustment, ending with the quality check of the results from the hybrid adjustment.

## 5.1. Data pre-processing

### 5.1.1. Pre-processing of LiDAR strips

The raw LiDAR measurements (.rdbx) files have been used in this research work as raw inputs for the LiDAR data. For the strip adjustment, “rdbx” files need to be converted to Opals Data Manager (.odm format) for the hybrid adjustment process. In the initial step, raw LiDAR measurements (.rdbx files) were converted to .odm format using the opalsImport module in Scanner Coordinate System (SCS) format. The “rdbx” files were categorized into 10 strips based on the initial dataset information and GPS time. The script for the conversion step has been provided in Table 9.1.

### 5.1.2. Pre-processing of camera images

The camera images with initial orientation parameters were processed in Agisoft Metashape software with the following parameters settings. The purpose of this processing is to export the tie object points and image point observations as inputs to the hybrid adjustment. The MetaShape project was transformed to input for strip adjustment with a python script API deriving the following files from an Agisoft Metashape project file.

- exterior image orientations
- image point observations for each photo containing
- tie object points

The following inputs/parameters were used to transform the Agisoft MetaShape project into the inputs of hybrid adjustment:

- Path of the MetaShape .psx project file
- Id of chunk to be imported
- Max Reprojection error
- Min Multiplicity
- output directory to store the files

### 5.1.3. Determination of time lag and sensor orientation on the UAS platform

For the hybrid adjustment process, the orientation of the LiDAR sensor on the platform and the time lag between the UAS platform and sensor observations need to be known in advance, which was not known for the datasets used in this research. The sensor orientation is the approximate direction of LiDAR sensor axes w.r.t the UAS-platform, restricted to Right Hand Systems (RHS). The approximate mounting of the LiDAR sensor on the UAS platform was determined by visualization of raw LiDAR strips in MATLAB. After obtaining the correct sensor orientation, the time lag was also determined with the plot of the input strip file with different time lag values in MATLAB. The sensor orientation was found to be urf (up/right/front) w.r.t. UAS-platform, and the time lag value was found to be -18 seconds. The time lag of -18 seconds attributes to the synchronization error between UAS-platform and LiDAR scanner, i.e., the UAS-trajectory time stamps lag by 18 seconds from the LiDAR scanner measurements, and these 18 seconds are to be added to the UAS-trajectory timestamps.

#### 5.1.4. Indexing of the images to LiDAR strips for hybrid adjustment with coupled images

In the case of hybrid adjustment with coupled images, every image is tied to a LiDAR strip via the common attribute "GPSTime." The images from the camera had image exposure time stamps "t," and LiDAR strips have the attribute "GPSTime." However, the LiDAR strips had GPSTime in GPS seconds of the day, whereas image timestamps were in GPSTime format. To unify the time for both images and LiDAR strips, GPS time of the day was subtracted from every image stamp value to obtain GPSTime.
For example, Image 1 from the dataset has timestamp "t" = 303203136.2, whereas LiDAR strip_1 has GPSTime from 31918.079 to 32311.642 GPS seconds. GPS time of the day was obtained for the data acquisition date 23rd April 2021 using a tool from (Laser Interferometer Gravitational-Wave Observatory, 2022) and subtracted from image time stamps to convert them to GPS seconds. For 23rd April 2021, GPSTime of the day was found to be 303171218 and subtracted to calculate timestamps in GPS seconds.
GPSTime for image 1 = (303203136.2 – 303171218 ) = 31918.2 GPS seconds which lies in the "GPSTime" range of strip_1 range. So, image 1 was indexed to strip_1, and a similar process was followed for other images

### 5.2. Processing of camera images before hybrid adjustment

The camera images were processed with the initial orientation parameters in Pix4D software with Dense Image Matching (DIM) and Structure from Motion (SfM) to generate a dense point cloud. The point cloud generated in this step is compared with the LiDAR point cloud to compute the discrepancies before the hybrid adjustment. The important calibration settings that should be taken care of in processing camera images are summarized in Table 5.1. Figure 5.1 represents the workflow for the processing of camera data before the hybrid adjustment to get a dense point cloud.

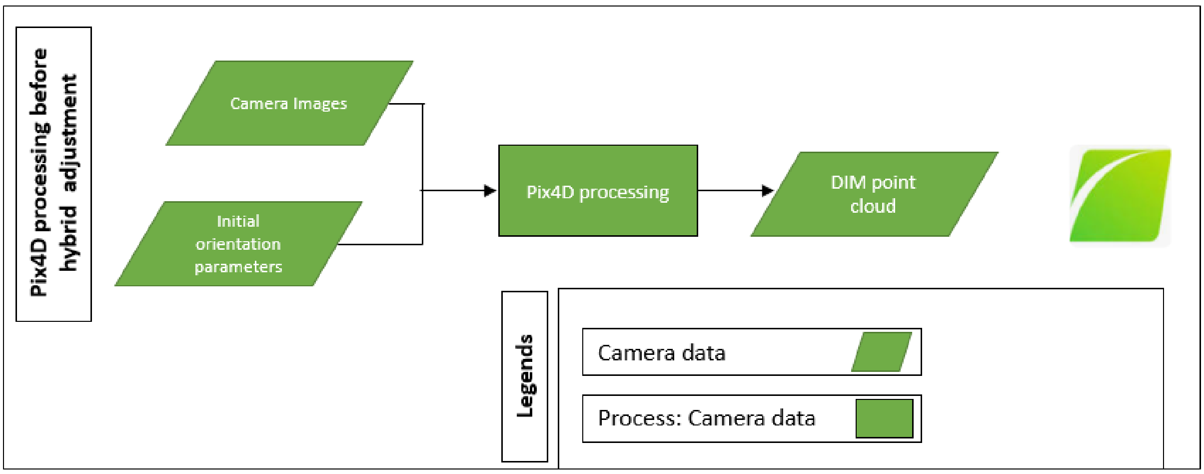


Figure 5.1: Pix4D processing of camera data before hybrid adjustment

Table 5.1: Calibration settings used in Pix4D processing of camera images before hybrid adjustment

| | |
|---|---|
| Targeted number of key points | Automatic |
| Calibration method | Accurate geolocation and orientation |
| Internal Parameters Optimization | None |
| External Parameters Optimization | None |

## 5.3. Hybrid adjustment with loose and coupled images

The hybrid adjustment of UAS-based camera data and LiDAR strips can be possible with two types of image inputs: one is loose images, and another is coupled images. In the case of hybrid adjustment with loose images, their relation to flight trajectory cannot be established because of the unavailability of timestamps for images. In this case, the exterior orientation parameters are directly estimated by the adjustment.

The coupled images are tied to the flight trajectory, and their exterior orientation can be estimated through the direct georeferencing equation as a function of UAS trajectory and camera mounting calibration parameters. The positional and rotational parameters obtained through the direct georeferencing equation can be inaccurate if the timestamps of images are inaccurate or residuals show systematic errors. Therefore, the exterior orientation is corrected by the three coordinate correction parameters and three rotational angle correction parameters in case of hybrid adjustment with coupled images. Figure 5.2 shows the difference between the loose and coupled images with respect to the UAS trajectory.

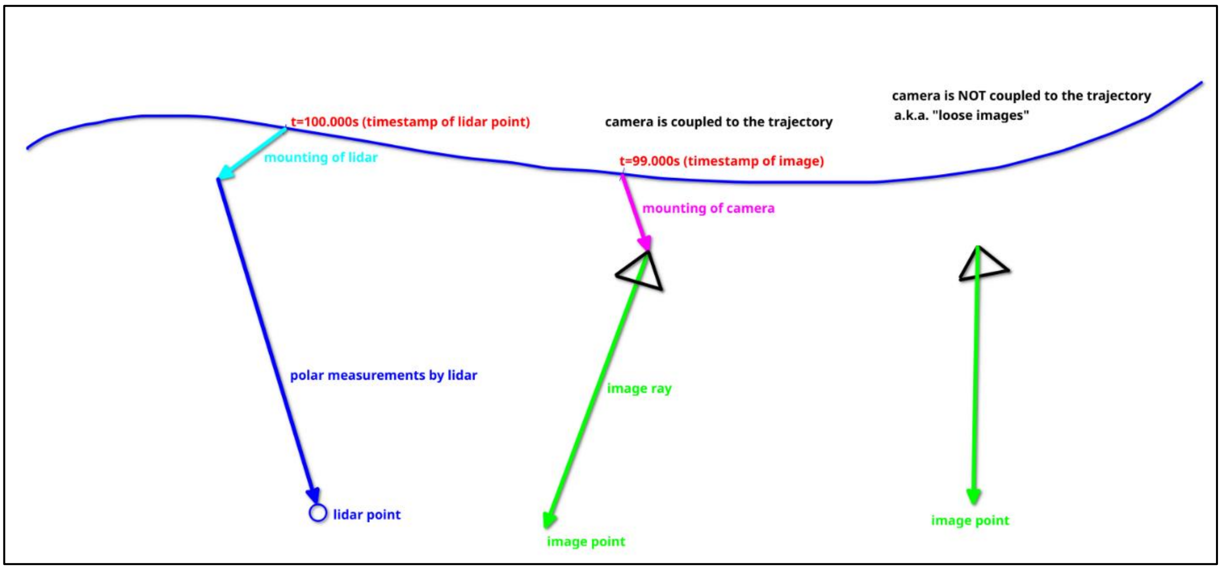


Figure 5.2: Illustration for loose and coupled images

The hybrid adjustment process starts with the image-based processing step. Initially, IMG-IMG correspondences are established in the first step. Then, aerial triangulation is implemented to estimate the 3D coordinates of the image tie points from the first step. The IMG-IMG correspondences established in this step are used in further steps of the hybrid adjustment. Then, the overlap between LiDAR strips (STR-STR) and (IMG-STR) are determined for the correspondences. After finding overlap, the query points are selected from STR-STR and IMG-STR correspondences with a uniform sampling technique, which selects the points from both the datasets in the object space as consistently as possible. The uniform sampling technique ensures that the uniform distribution of points in the correspondences and equal-area regions are weighted equally within the hybrid adjustment.

The main iteration loop in the hybrid adjustment starts with the direct georeferencing of the LiDAR strips (with the initial parameters in the first loop and estimated parameters from the hybrid adjustment in the subsequent loops). The potential correspondences are matched, i.e., the nearest neighbor of a query point in the overlapping point cloud. The false correspondences are rejected and removed in the subsequent step based on roughness criteria, the distance between the corresponding points, and the threshold angle between the normals of the corresponding points. The correspondences that remained after the rejection step are weighted based on their surface roughness and angle between respective surface normals. It is worth mentioning that the correspondences are also newly established in each iteration of hybrid adjustment. After a given number of iterations are completed (usually 5 are enough), the LiDAR strips are georeferenced with the estimated parameters in the final iteration loop of the hybrid adjustment. The workflow for the hybrid adjustment in Opals is shown in Figure 5.3.

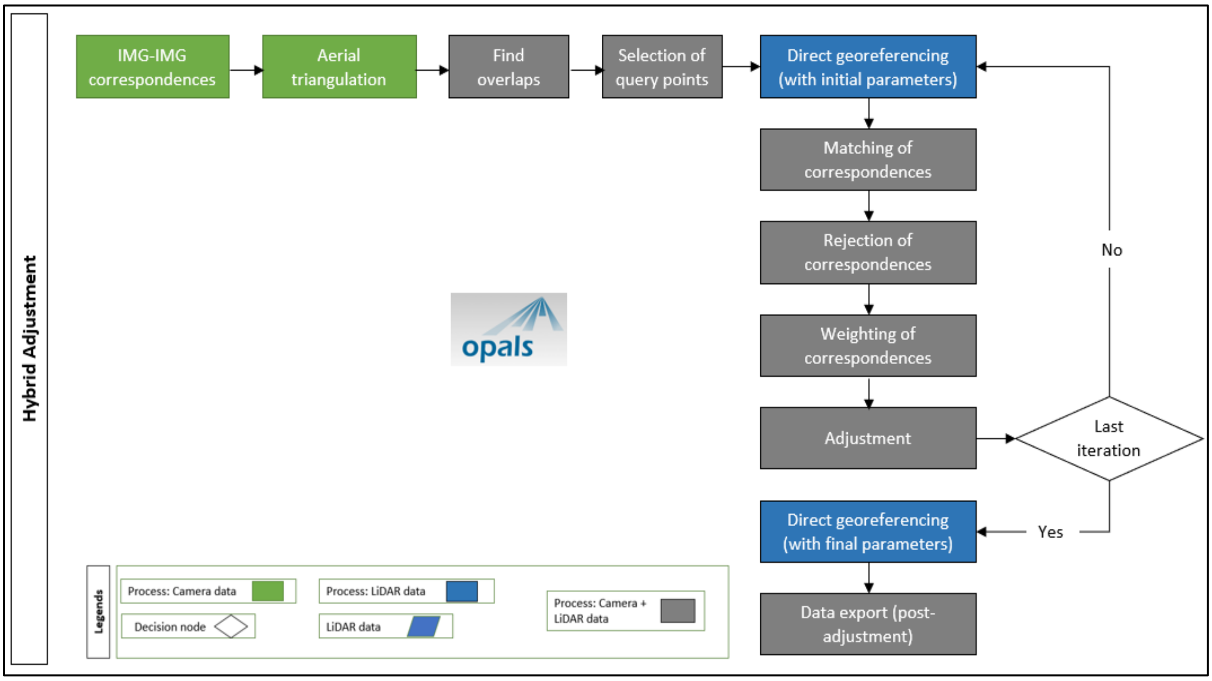

Figure 5.3: Workflow for the hybrid adjustment process in Opals

In the hybrid adjustment, the least square adjustment minimizes the weighted square sum for the following types of correspondences:

- IMG-IMG: reprojection errors of image tie points in the image space
- STR-STR: signed perpendicular point-to-plane distances between overlapping LiDAR strips
- IMG-STR: signed perpendicular point-to-plane distances between image tie points and overlapping LiDAR strips

The data outputs from the hybrid adjustment with the loose and coupled images are as follows:

- Calibrated LiDAR strips
- Undistorted images
- Estimated orientation parameters of undistorted images
- Flight strip trajectories w.r.t. INS/scanner coordinate system
- Report file of the hybrid adjustment process

### 5.4. Parameters used in the hybrid adjustment

The hybrid adjustment in Opals stripAdjust module was implemented with the different parameters as it was originally designed for the ALS-based datasets. The difference in the case of the UAS-based datasets that the planes extracted for the matching of the LiDAR and camera datasets would be larger as compared to ALS-based datasets. The main parameters considered in the hybrid adjustment approach are listed as follows:

- UTM zone information on UTM projection of the datasets
- Hemisphere within the UTM zone (north/south)
- Size of the edge length of voxel to find overlap between points from datasets
- Max. no. of iterations for hybrid adjustment
- Orientation of LiDAR sensor w.r.t. UAS-platform
- Trajectory correction model to be used in the hybrid adjustment
- Length of time segments to estimate trajectory correction functions
- Standard deviation of trajectory observations
- Search radius for plane fitting to estimate normal vector in one point
- Minimum number of neighbors for the normals estimation
- Time lag between LiDAR scanner observations and UAS-trajectory
- Standard deviation of image observations
- Focal length of the camera
- Principal point coordinates
- Minimum number of overlapping pixels
- Sampling distance and radius for subset points selection
- Threshold distance between corresponding points for correspondence rejection
- Priori point-to-plane distance between image tie points and LiDAR strips

The parameters and the values used in the hybrid adjustment with loose and coupled images can be found in Table 9.2.

### 5.5. Processing of camera images after hybrid adjustment

The undistorted images and estimated orientation parameters from the hybrid adjustment are used for the post-processing of the camera dataset. The purpose of this step is to generate Dense Image Matching (DIM) point cloud from the distortion-free images and parameters post hybrid adjustment. The main factor considered here is that calibration was restricted to the accurate geolocations estimated by hybrid adjustment.

The principal point coordinates obtained from the hybrid adjustment need to be converted to Pix4D because of the different coordinate system of Opals for the hybrid adjustment. The principal point coordinates from the hybrid adjustment $(x_h, y_h)$ were converted to pix4D coordinates $(x_o, y_o)$ by the equations 5.1 and 5.2.

$$x_o = [x_h - 0.50] \tag{5.1}$$
$$y_o = [-(y_h) - 0.50] \tag{5.2}$$

The further optimization of internal and external orientation parameters was disabled during the DIM process to get the point cloud with the same parameters estimated from the hybrid adjustment. Similar settings, as mentioned in Table 5.1, were used for the processing of camera images after hybrid adjustment. The input and output coordinate system for the dataset processing is ETRS89/ UTM 32N.

The workflow for the post-processing of camera data after hybrid adjustment to get a dense point cloud is shown below in Figure 5.4.

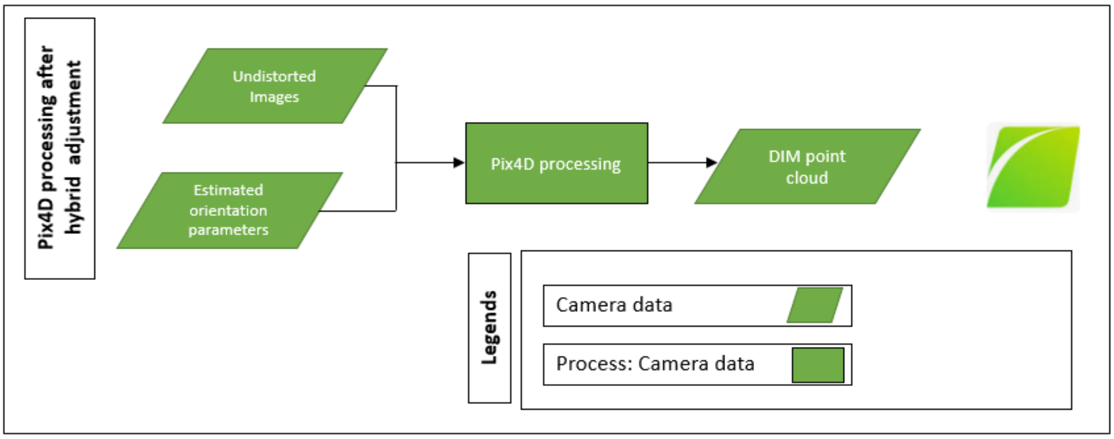


Figure 5.4: Pix4D processing of the camera data after hybrid adjustment

## 5.6. Quality check

Two methods have been used in this research work for the quality check of the results after hybrid adjustment: Cloud-to-Cloud distances and DSM-based height differences. The description of these quality checks has been explained in the following sub-sections.

### 5.6.1. Cloud-to-Cloud distamces (C2C distances)

The cloud-to-cloud distances have been computed between the LiDAR point cloud after hybrid adjustment and the DIM point cloud generated from the undistorted images and orientation parameters estimated from the hybrid adjustment. This C2C distance method gives the distance differences between two-point clouds based on the nearest neighbor distance between two-point clouds. For the computation, one point cloud is to be defined as a "reference" point cloud (usually with higher point density) and the other as "compared" for which the distances have to be computed. For every point in the "compared" point cloud, the algorithm search for its nearest point in the "reference" point cloud, and the Euclidean distances between the nearest neighbor points are computed (Ahmad Fuad et al., 2018).

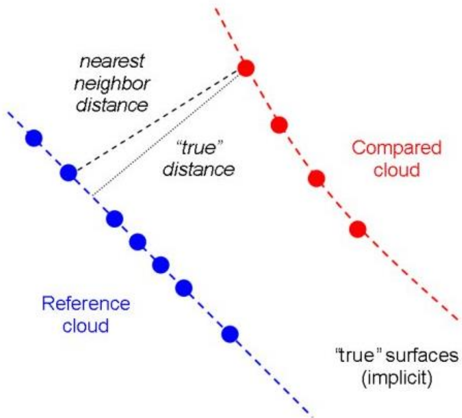


Figure 5.5: Principle of cloud-to-cloud distance computation (CloudCompare, 2021)

In the absence of any local surface model, the C2C distance is simply the nearest neighbor distance computed using a Hausdorff algorithm. The Hausdorff algorithm simply computes the distance between all the corresponding points in two-point clouds. The Hausdorff distance from a set of points P to another set Q is given by (Ahmad Fuad et al., 2018) :

$$H\,(P, Q) = max_{p \in P}\left\{min_{q \in Q}\,\{d(p, q)\}\right\} \tag{5.3}$$

where

- $p$ are points in set P
- $q$ are points in set Q
- $d(p, q)$ is any metric for these points $p$ and $q$

The demerit of simply computing C2C distances is that the nearest neighbor is not mandatorily the actual nearest point on the "reference" point cloud surface. To ensure this, a local surface modelling strategy around the nearest point was chosen to better approximate the exact and true distances to the compared point cloud surface. The computation principle of the local surface model is based on the locally modeled "reference" point cloud surface by fitting a statistical model on the nearest point and its neighbors. Three local surface models are available in the CloudCompare software, namely least square plane, 2DI/2 Triangulation, and Quadric, in their increasing order of computation time. The "Quadric" local surface model was used in C2C distance computations to get a better approximation of the distances between the point clouds.

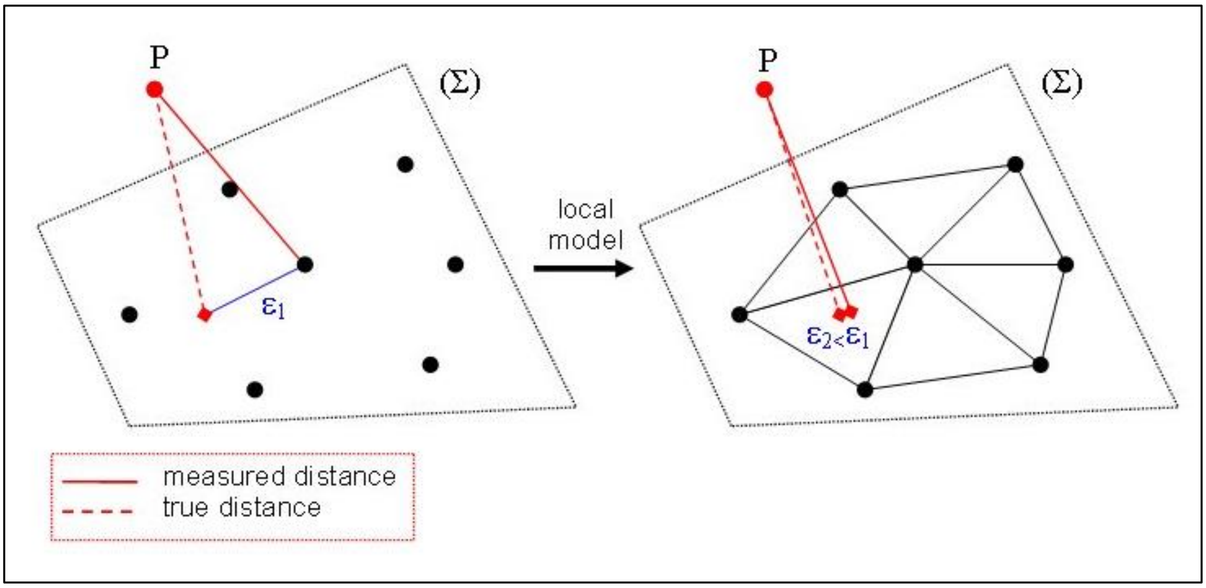


Figure 5.6: Principle of C2C distances computation with the local surface modeling (CloudCompare, 2021)

The C2C distances were compared for the point clouds before and after hybrid adjustment to analyze the improvements in the alignment of point clouds with the hybrid adjustment. The C2C distances were computed with the LiDAR point cloud as "reference" and the DIM point cloud as "compared" entities. The local modelling strategy with a versatile quadric model was used to compute C2C distances along the smooth and curvy edges in the point clouds.

#### 5.6.2. DSM-based height differences (OpalsQuality check)

OpalsQuality (Pfeifer et al., 2014) is a package in the Opals modular program that provides an end-to-end processing chain for the quality assessment of the overlapping point clouds. It calculates DSMs for the overlapping point clouds and estimates their relative height differences. Point clouds were converted to

ODM format for this quality check method, a pre-requisite for Opals processing. After DSM computation, Opals Quality check gives the relative height differences by the raster subtraction of (DSM_2) from (DSM_1). The color-coded differences between the overlapping point clouds were finally obtained along with the statistics for their relative height differences.

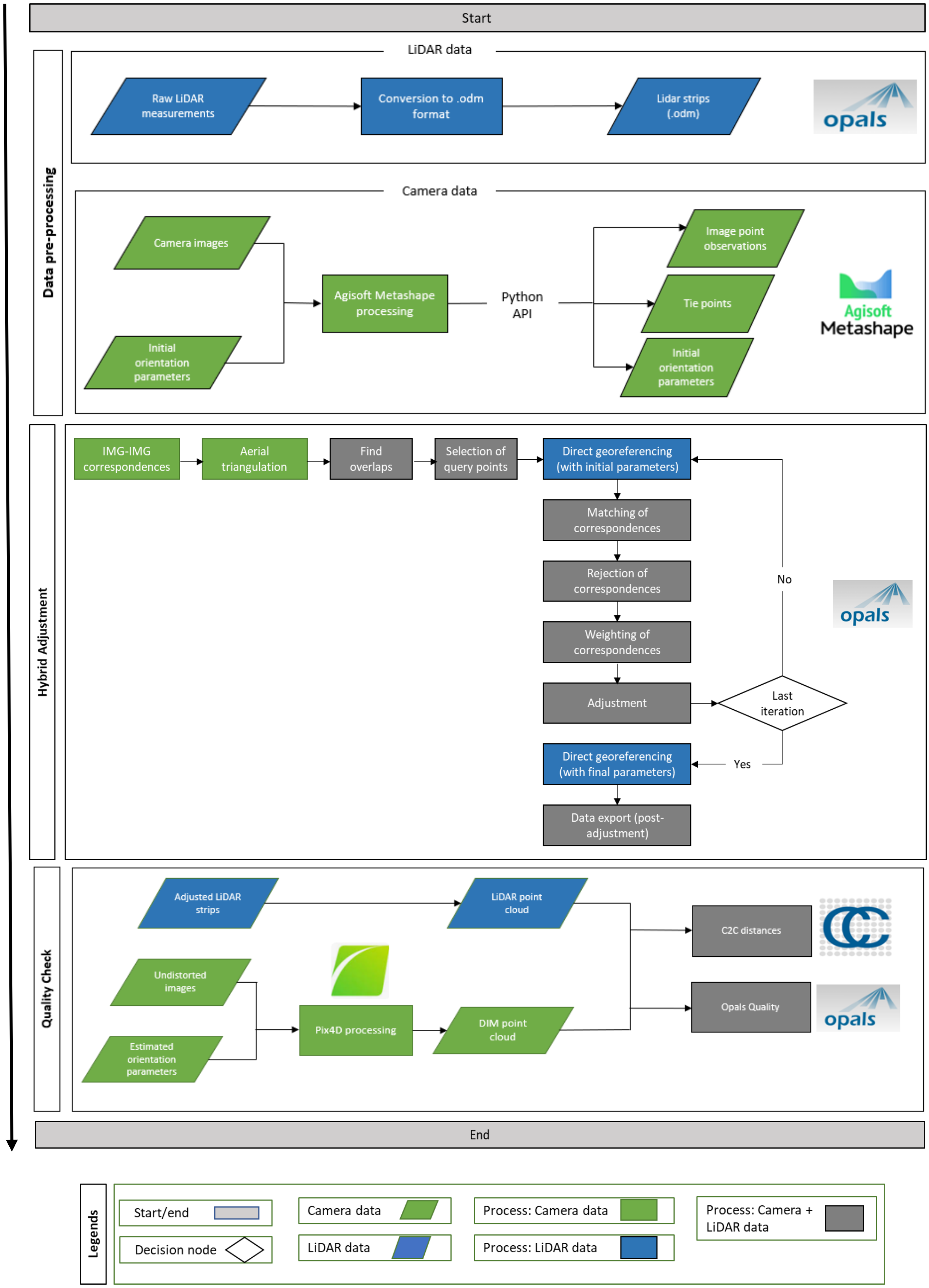


Figure 5.7: Complete methodology workflow for the hybrid adjustment approach

# 6. RESULTS AND DISCUSSIONS

This chapter comprises the results from the hybrid adjustment process and their comparison with the dataset before the adjustment. This chapter also indicates how the hybrid adjustment approach has improved the results for the orientation between LiDAR and images-derived DIM point clouds.

## 6.1. Generation of point clouds from camera images

The initial point cloud was generated from the camera images and initial orientations to compare with LiDAR point clouds before the adjustment. After the hybrid adjustment, the point cloud was generated from the undistorted images and estimated orientations for the comparison with the adjusted LiDAR point clouds. To maintain homogeneity in the comparison, the same settings and parameters were used for the processing of camera images in Pix4DMapper software before and after hybrid adjustment. The settings were kept the same for processing the camera images before and after the hybrid adjustment

## 6.2. C2C differences between LiDAR point cloud and DIM point cloud (at dataset level)

For dataset_A, the hybrid adjustment was experimented with loose and coupled images using bias and linear trajectory correction models. The C2C distances were computed between the LiDAR point cloud and the DIM point cloud generated from the camera images before and after the hybrid adjustment. The C2C distances were computed with the LiDAR point cloud as “reference” and the DIM point cloud as a “compared” entity for all the comparisons due to the reliability and higher number of points in LiDAR point clouds. The local modeling strategy with a versatile “quadric” model was used to compute C2C distances along the smooth and curvy edges in the point clouds. The higher standard deviation in the statistics is due to the higher number of points in the LiDAR point cloud for which there are very few or no corresponding points in the DIM point cloud for C2C distance computation. The computed C2C distances and standard deviations before and post-hybrid adjustment are summarized in Table 6.1 and Figure 6.1.

Table 6.1: Mean C2C distances between LiDAR and DIM point clouds for dataset_A

| | | **Bias trajectory correction model** | | **Linear trajectory correction model** | |
|---|---|---|---|---|---|
| Parameter | Before hybrid adjustment | Adjustment with loose images | Adjustment with coupled images | Adjustment with loose images | Adjustment with coupled images |
| Mean C2C distance (m) | 1.172 | 0.091 | **0.088** | 0.090 | 0.089 |
| Standard deviation (m) | 0.194 m | 0.271 | **0.269** | 0.275 | 0.272 |

From the results in Table 6.1, the mean C2C distance between LiDAR and DIM point cloud was 1.172 m, and after hybrid implementation with loose and coupled images using bias and linear trajectory correction models, the mean C2C distances came down to the sub-centimeter range. The hybrid adjustment with coupled images and bias trajectory correction model resulted in the least mean C2C distances, i.e., the orientation of LiDAR and camera dataset was adjusted with the least errors by hybrid adjustment with coupled images using a bias trajectory correction model. The higher standard deviation in C2C distances can be attributed to different point densities of LiDAR and DIM point clouds, noise in the point clouds, and possible differences in the coverage of the point clouds. The other reason can be given by the penetration capability of LiDAR through some surfaces like vegetation and transparent surfaces where LiDAR would have points, and DIM point cloud would not have any points. So, the absence of corresponding points would lead to a higher standard deviation in C2C distances.

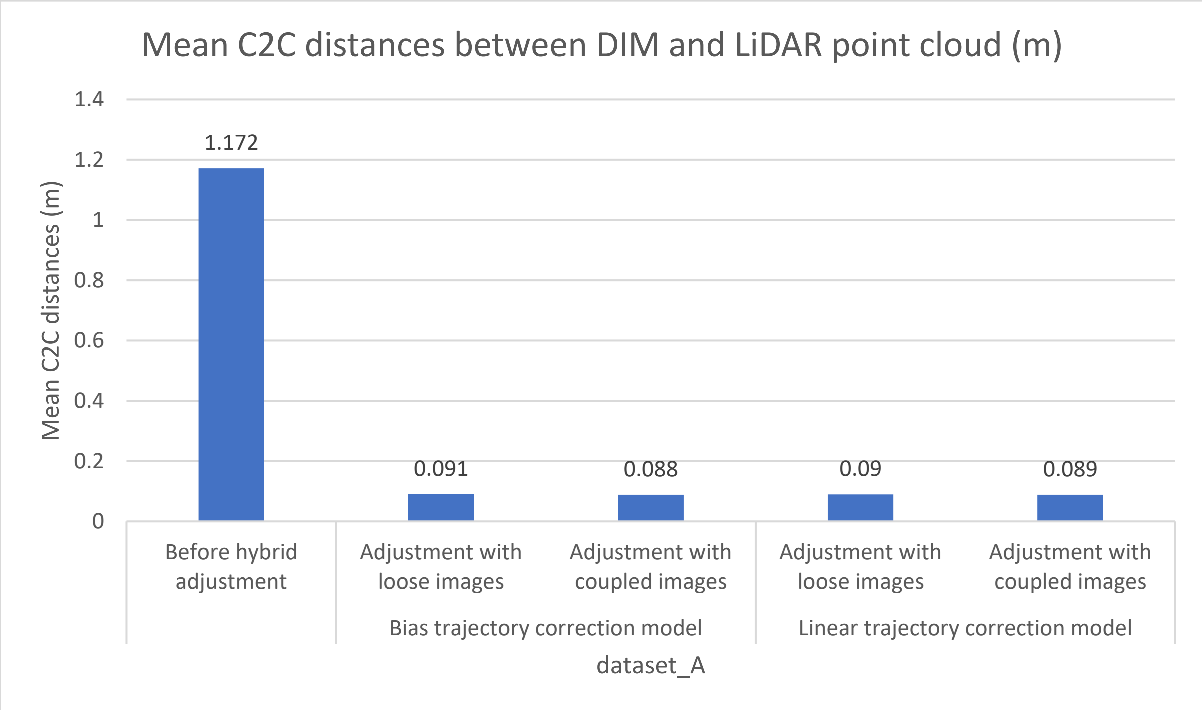


Figure 6.1: Bar plot representing mean C2C distances between DIM and LiDAR point cloud for dataset_A

Table 6.1 and Figure 6.1 implies that the hybrid adjustment with coupled images and bias trajectory correction model results in the least C2C distances between LiDAR and DIM point clouds compared to hybrid adjustment with loose images and combination with linear trajectory correction model.
Figure 6.2 shows the C2C distances between LiDAR and DIM point clouds from dataset_A within the range of 10 cm, represented by an active scalar field (RGB), whereas points with C2C distances higher than 10 cm are in grey. Here, the 10 cm range implies the C2C distances between 0 and 10 cm. The value of 10 cm was chosen for the comparison because the average mean C2C distances after hybrid adjustment were ~ 10 cm, and this value would give a better visual interpretation of the performance of the hybrid adjustment approach. From Figure 6.2, it is evident that very few points or regions with C2C distances are within 10 cm, and after hybrid adjustment, there were relatively higher points with C2C distances within the 10 cm range. It is distinguishable that C2C distances have been reduced significantly after the hybrid adjustment implementation. The regions or the points in RGB are those where mean C2C distances between LiDAR and DIM point clouds are less than 10 cm, whereas for the regions in grey, mean C2C distances are higher than 10 cm.

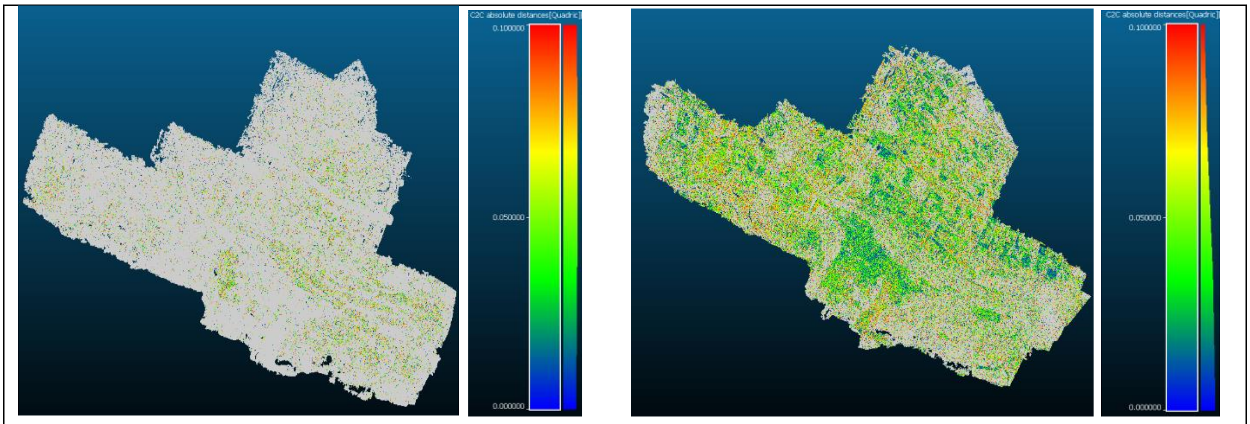

a) Before hybrid adjustment b) After hybrid adjustment

Figure 6.2: C2C distances between LiDAR and DIM point clouds (with 10 cm range) for dataset_A

For the dataset_A, the hybrid adjustment was implemented with loose and coupled images using bias and linear trajectory correction models. From the results of dataset_A, it was observed that the most accurate orientation between LiDAR and camera point clouds could be achieved from the hybrid adjustment with coupled images and a bias trajectory correction model. So, for the dataset_B and dataset_C, the hybrid adjustment was implemented with coupled images case only with a bias trajectory correction model to check the compatibility and performance of the hybrid adjustment process on the other datasets as well. The purpose is to ensure that the hybrid adjustment workflow should work well for other datasets and check the results of the hybrid adjustment for different datasets. The hybrid adjustment was implemented, and the C2C distances were computed similarly for dataset_B and dataset_C. The results of the hybrid adjustment implementation for dataset_B are summarized in Table 6.2.

Table 6.2: Mean C2C distances and standard deviation for dataset_B

| Parameter | Before hybrid adjustment | After hybrid adjustment with coupled images |
|---|---|---|
| Mean C2C distances (m) | 0.268 | 0.085 |
| Mean standard deviation (m) | 0.935 | 0.383 |

From the results analysis of the dataset_B, the initial discrepancies between the LiDAR and DIM point clouds were found to be 0.268 m (~ 27 cm), and after hybrid adjustment with the coupled images, discrepancies were minimized to 0.085 m (8.5 cm). The higher standard deviation in C2C distances can be attributed to the higher number of points in LiDAR point cloud w.r.t. DIM point cloud and maybe some noise around the point clouds for which the computed C2C distances would be exceptionally higher. The bar plot in Figure 6.3 shows the improvement in the orientation of LiDAR and DIM point cloud post hybrid adjustment. For the visual interpretation, the C2C distances between LiDAR and DIM point clouds within a range of 10 cm were also compared in figure 6.4 before and after hybrid adjustment. The RGB scalar field shows the C2C distances within the 0 to 10 cm range, whereas C2C distances above 10 cm are in greyscale. The higher number of points within the 10 cm range can be observed in the point clouds after hybrid adjustment, which indicates the better orientation of LiDAR and DIM point clouds after hybrid adjustment.

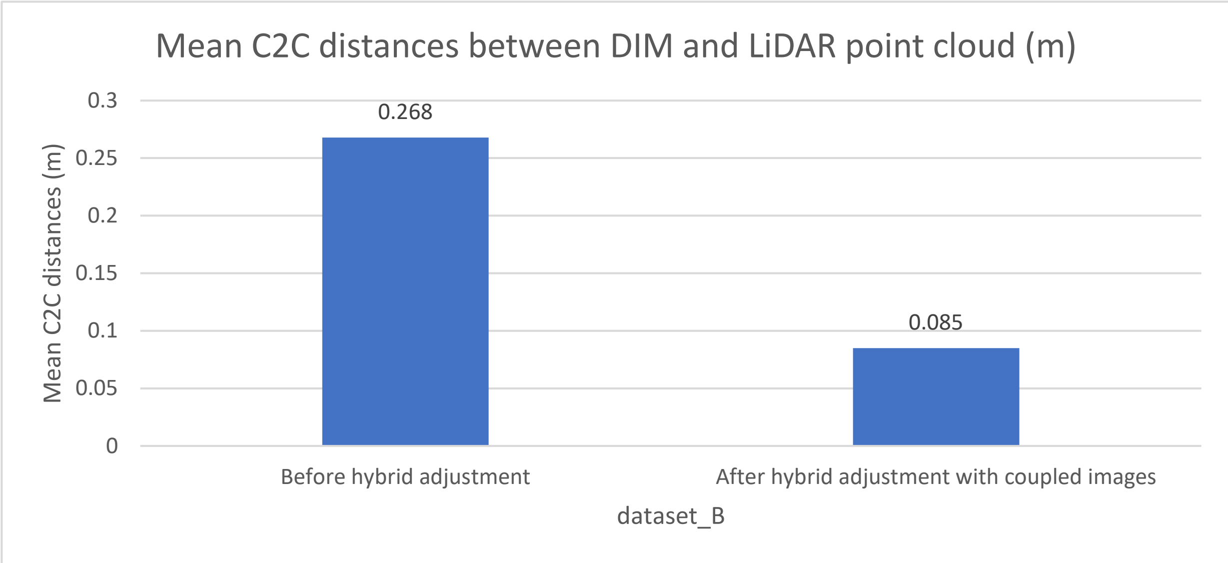


Figure 6.3: Bar plot representing mean C2C distances between DIM and LiDAR point cloud for dataset_B

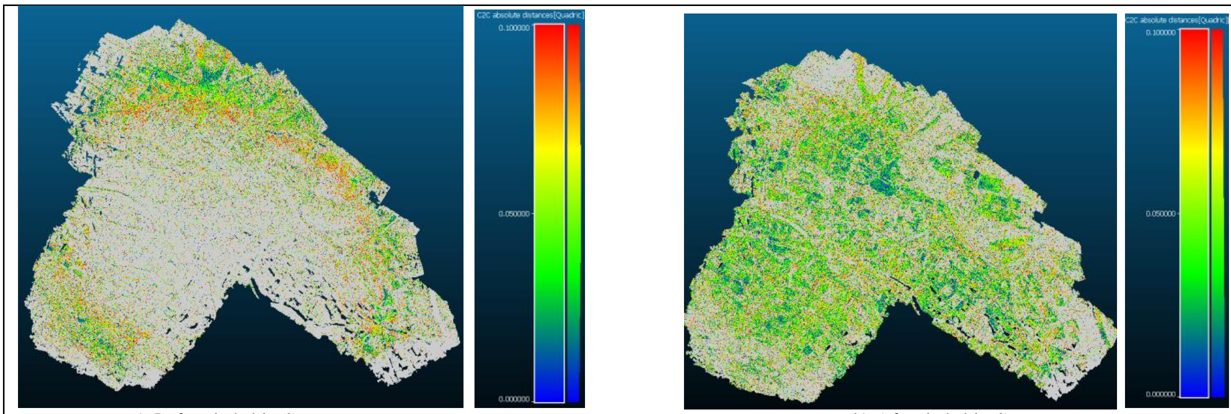

a) Before hybrid adjustment b) After hybrid adjustment

Figure 6.4: C2C distances (with 10 cm range) between LiDAR and DIM point clouds for dataset_B

Similar to dataset_B, the hybrid adjustment was implemented for the dataset_C with coupled images, and C2C distances were compared before and after the hybrid adjustment. The mean C2C distances and the standard distances for the dataset_C are summarized in Table 6.3.

Table 6.3: Mean C2C distances and standard deviation for dataset_C

| | Before hybrid adjustment | After hybrid adjustment with coupled images |
|---|---|---|
| Mean C2C distances (m) | 0.483 | 0.067 |
| Mean standard deviation (m) | 0.872 | 0.294 |

The initial mean C2C distances for the dataset_C were 0.483 m (~48 cm) and reduced to 0.067 m ( 6.7 cm) after hybrid adjustment. The results can be clearly interpreted in Figure 6.5 and Figure 6.6.

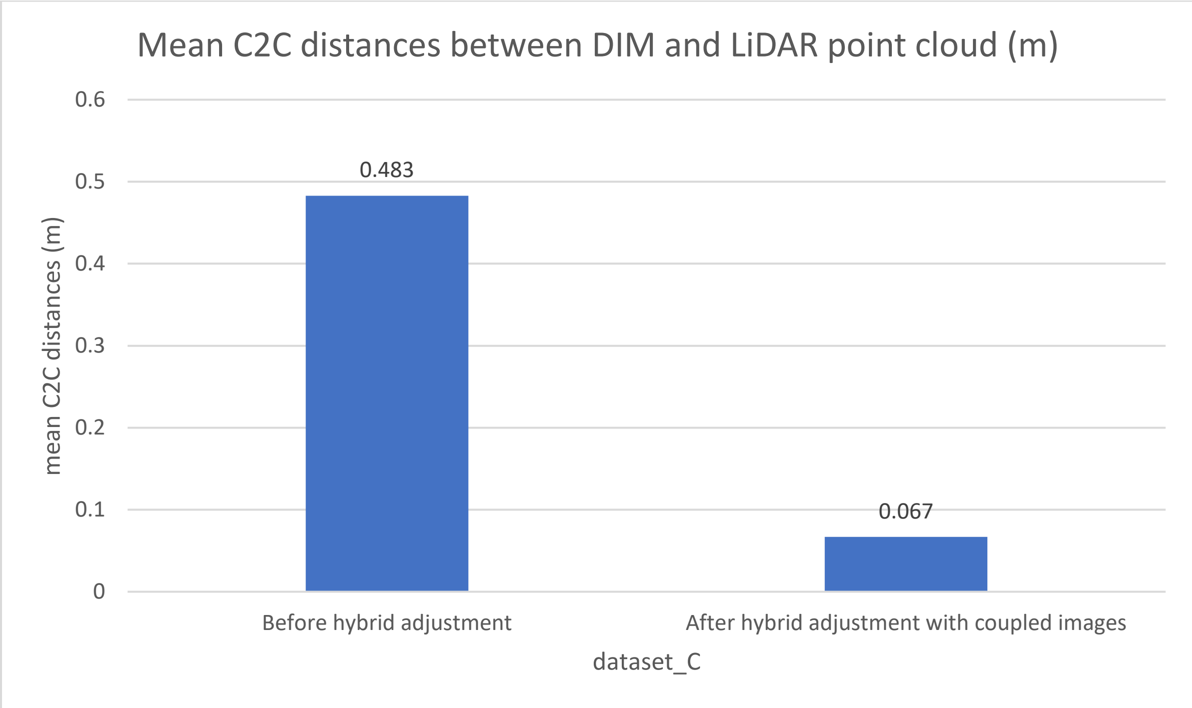


Figure 6.5: Bar plot representing mean C2C distances between DIM and LiDAR point cloud for dataset_C

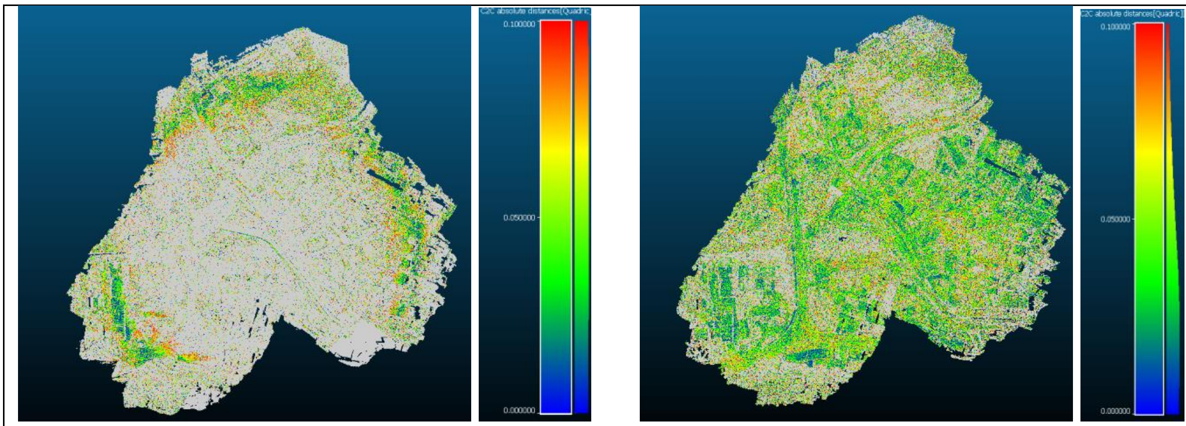

a) Before hybrid adjustment b) After hybrid adjustment

Figure 6.6: C2C distances (with 10cm range) between LiDAR and DIM point clouds for dataset_C

The plot in Figure 6.7 shows the overall performance of the hybrid adjustment approach for the dataset_A, dataset_B, and dataset_C. The mean C2C distances before hybrid adjustment were represented on the primary Y-axis (on the left) and mean C2C distances after hybrid adjustment are represented on the secondary Y-axis (on the right) in the plot in Figure 6.7.

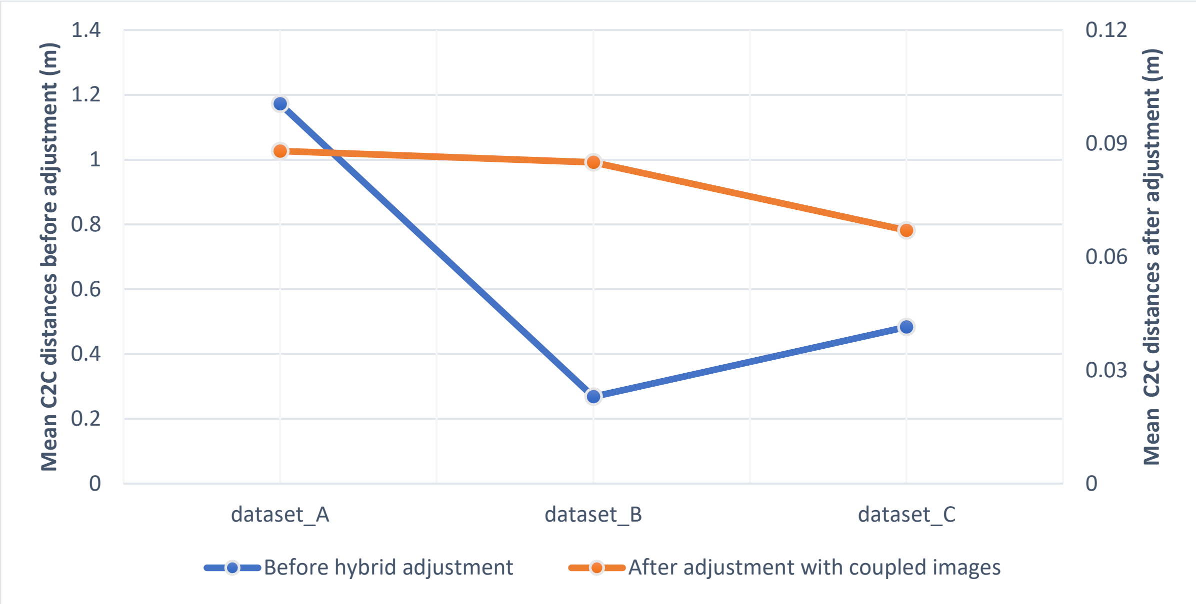


Figure 6.7: Mean C2C distances between DIM and LiDAR point cloud for dataset_A, dataset_B and dataset_C

The results indicate that the hybrid adjustment approach successfully minimizes the discrepancies between UAS-based LiDAR and camera datasets, and the implemented method has potentially reduced the discrepancies between LiDAR and camera datasets to a sub-centimeter range.

### 6.3. C2C distances between different surfaces from LiDAR and DIM point cloud (surface-level analysis)

There can be uncertainties in the dataset level C2C distance computations between LiDAR and DIM point clouds due to the different sensor characteristics of LiDAR and camera sensors. These uncertainties in the mean C2C distances can also be due to different point densities of LiDAR and DIM point clouds. The primary reason for it is the higher number of points in LiDAR and its penetration capability through the surfaces. LiDAR sensors with the penetration capability can also include points through the surfaces like grass, and transparent glass, whereas DIM point clouds only cover the top part of the surfaces. So, surface-level analysis can better interpret mean C2C distances before and after hybrid adjustment. So, five types of surfaces from the study area were identified from all three datasets (dataset_A, dataset_B, and dataset_C) for the surface level C2C distance analysis. The identified surfaces were the flat roof, slant roof, road surface, bare land, and road surface. The C2C distances before and after hybrid adjustment were computed between the different types of surfaces from both the point cloud datasets for the surface level analysis. The planar roof, slant roof, bare land, road, and vegetation surfaces were segmented using the "segment" tool in Cloud Compare software. It is worth mentioning that similar surfaces with the same extent and coverage were compared here for C2C distances before and after hybrid adjustment. Like the C2C distance computation in section 6.2, the local model "quadric" was used here. The location of different surfaces from dataset_A used for the surface-level analysis of mean C2C distances is shown in Figure 6.8. The mean C2C distances between different surfaces from dataset_A are summarized in Table 6.4. The mean C2C distances were lower at the surface level for the planar roof, slant roof, road, and bare land surfaces (<0.088 m), whereas for the vegetation surface, mean C2C distances are higher (> 0.088 m) as compared to mean C2C distances at dataset level (0.088 m). The higher mean C2C distances in the vegetation surfaces can be due to the higher penetration capability of the LiDAR sensor through the vegetation resulting in higher points compared to the DIM point cloud.

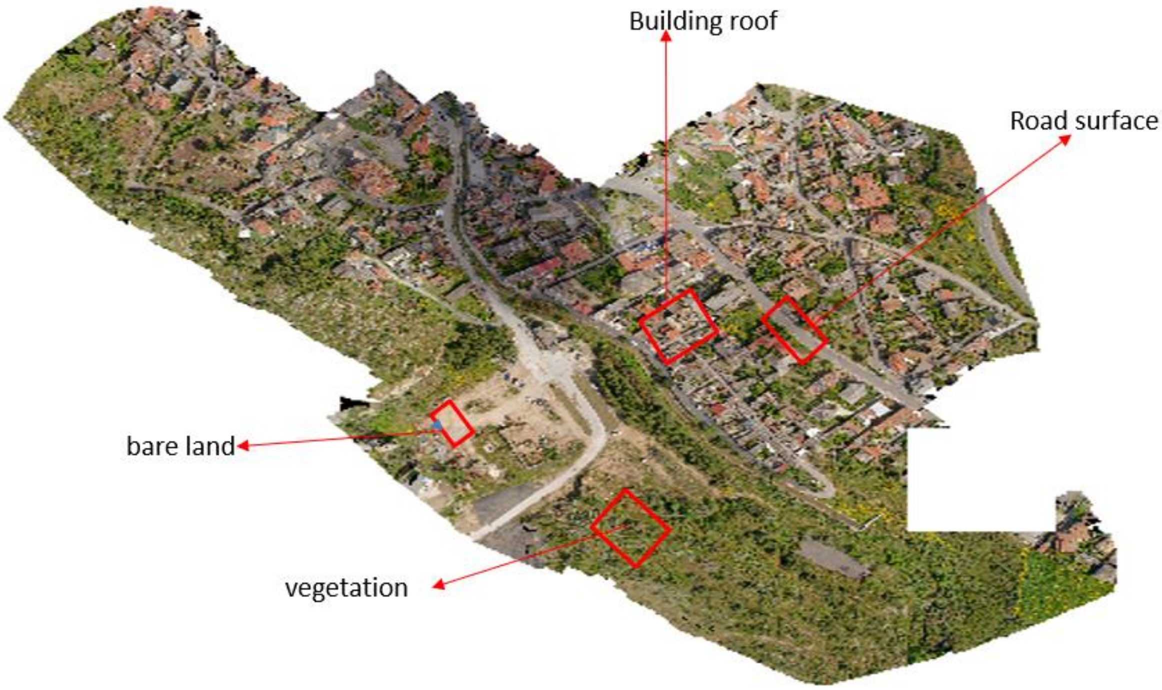


Figure 6.8: Location of different surfaces from dataset_A used for the surface-level analysis of mean C2C distances

Table 6.4: Mean C2C distances for different surfaces from LiDAR and DIM point cloud of dataset_A

| Surface type | Mean C2C distances (m) | |
|---|---|---|
| | Before hybrid adjustment | After hybrid adjustment with coupled images |
| Planar roof | 1.283 | 0.042 |
| Slant roof | 1.168 | 0.036 |
| Bare land | 1.865 | 0.037 |
| Road | 1.698 | 0.045 |
| Vegetation | 0.971 | 0.112 |

Like dataset_A, the mean C2C distances were also analyzed for different surfaces from dataset_B and dataset_C. The location of different surfaces from dataset_B considered for the mean C2C distances analysis are shown in Figure 6.9. The results from the dataset_B followed a similar trend as dataset_A, which are summarized in Table 6.5. The planar roof, slant roof, roof, and bare land surfaces have mean C2C distances lower (<0.085 m) than the mean C2C distances dataset level (0.085 m). The mean C2C distances for the vegetation surface were higher than the dataset level (>0.085 m).

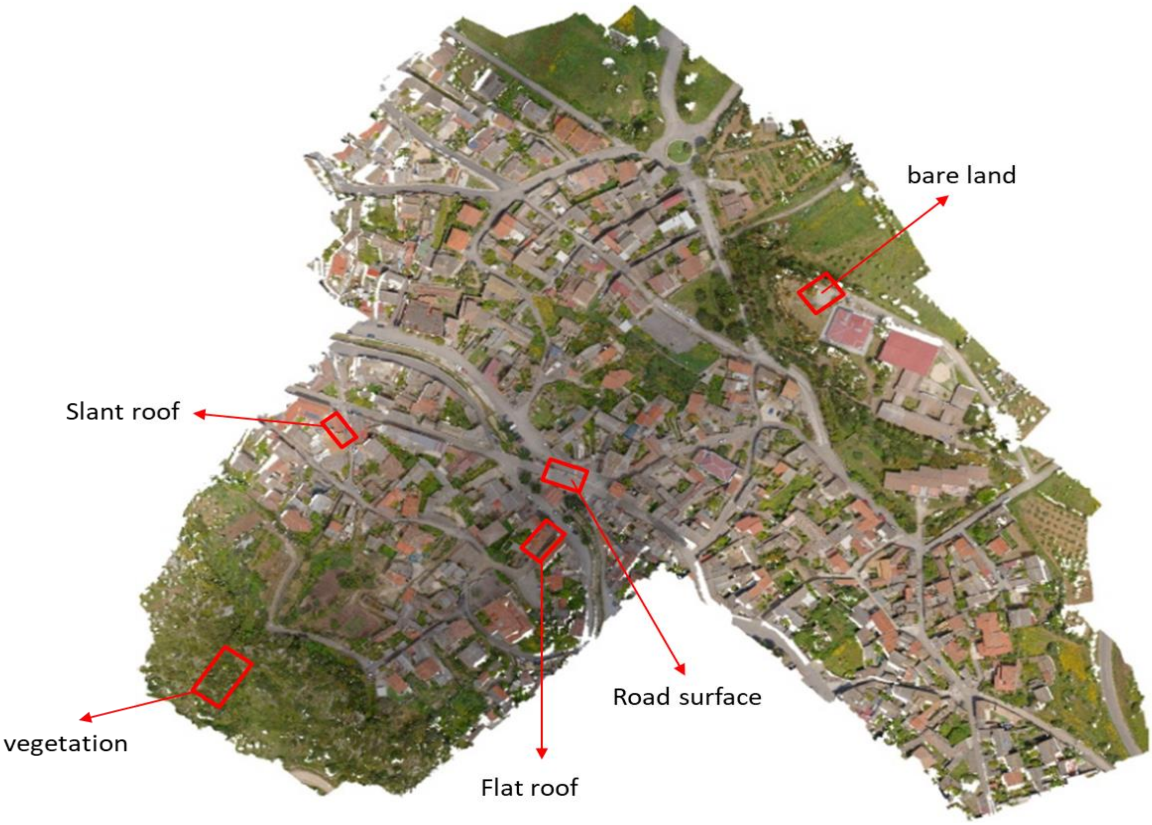


Figure 6.9: Location of different surfaces from dataset_B used for the surface-level analysis of mean C2C distances

Table 6.5: Mean C2C distances for different surfaces from LiDAR and DIM point cloud of dataset_B

| Surface type | Mean C2C distances (m) | |
|---|---|---|
| | Before hybrid adjustment | After hybrid adjustment with coupled images |
| Planar roof | 0.242 | 0.041 |
| Slant roof | 0.279 | 0.054 |
| Bare land | 0.341 | 0.049 |
| Road | 0.311 | 0.044 |
| Vegetation | 0.324 | 0.096 |

Figure 6.10 shows the location of different surfaces from dataset_C, which were considered for the surface-level analysis. From the results of the surface-level analysis of dataset_C in Table 6.6, the surface-level mean C2C distances were less than the mean C2C distances at the dataset level except for the vegetation surface. From the analysis of the three datasets, it can be concluded that the mean C2C distances at the surface level give a better estimate of the orientation before and after hybrid adjustment because of the computation of C2C distances at the exact surface level. At the dataset level, there is a possibility of different point densities at different locations, contributing to the higher mean C2C distances for the entire dataset.

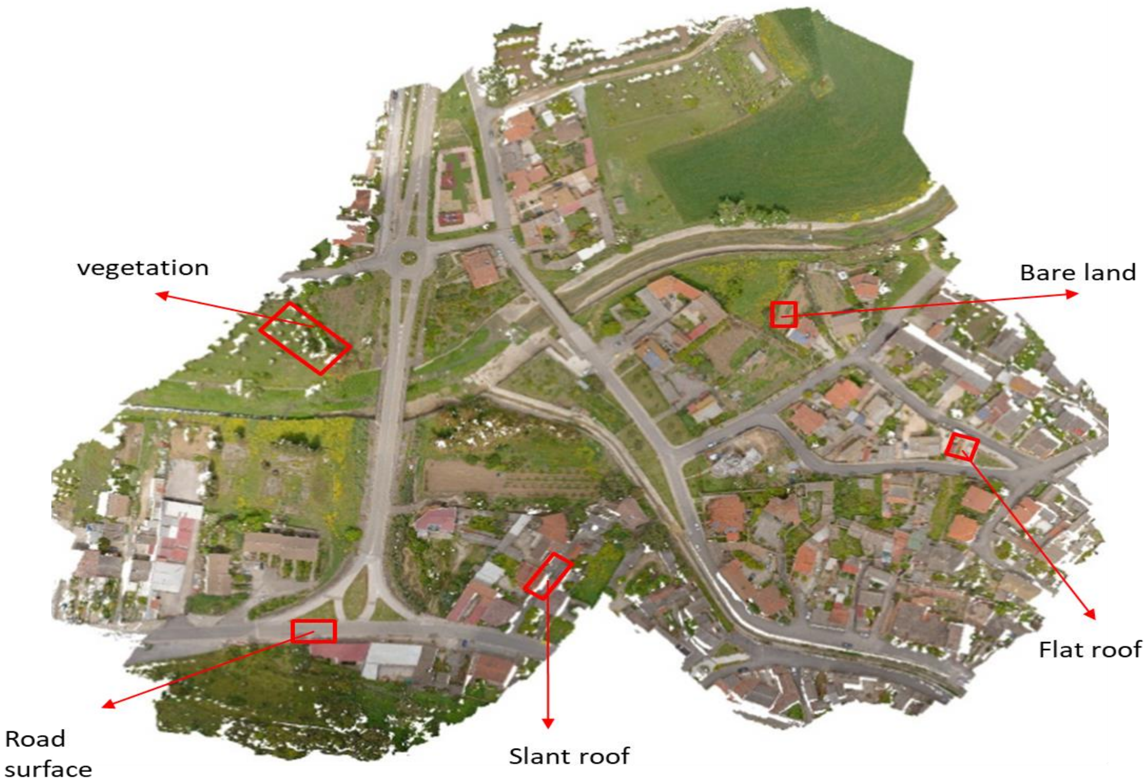


Figure 6.10: Location of different surfaces from dataset_C used for the surface-level analysis of mean C2C distances

Table 6.6: Mean C2C distances for different surfaces from LiDAR and DIM point cloud of dataset_C

| Surface type | Mean C2C distances (m) | |
|---|---|---|
| | Before hybrid adjustment | After hybrid adjustment with coupled images |
| Planar roof | 0.268 | 0.035 |
| Slant roof | 0.299 | 0.043 |
| Bare land | 0.364 | 0.048 |
| Road | 0.381 | 0.038 |
| Vegetation | 0.422 | 0.088 |

The bar plot in Figure 6.11 shows the mean C2C distances for different surfaces from dataset_A, dataset_B, and dataset_C before and after hybrid adjustment. For all three datasets, the mean C2C distances have been reduced from the range of meters to a few centimeters. Also, the mean C2C distances were lower than the mean C2C distances for the entire dataset level for the planar roof, slant roof, road, and bare land surfaces, whereas it was higher for the vegetation surfaces in all three datasets. The surface-level mean C2C distances are a better measure of discrepancies as the distances are computed exactly at the surface level without considering any noise or outliers. In both the dataset and surface-level analysis, the discrepancies were observed to be reduced to a sub-centimeter level post hybrid adjustment.

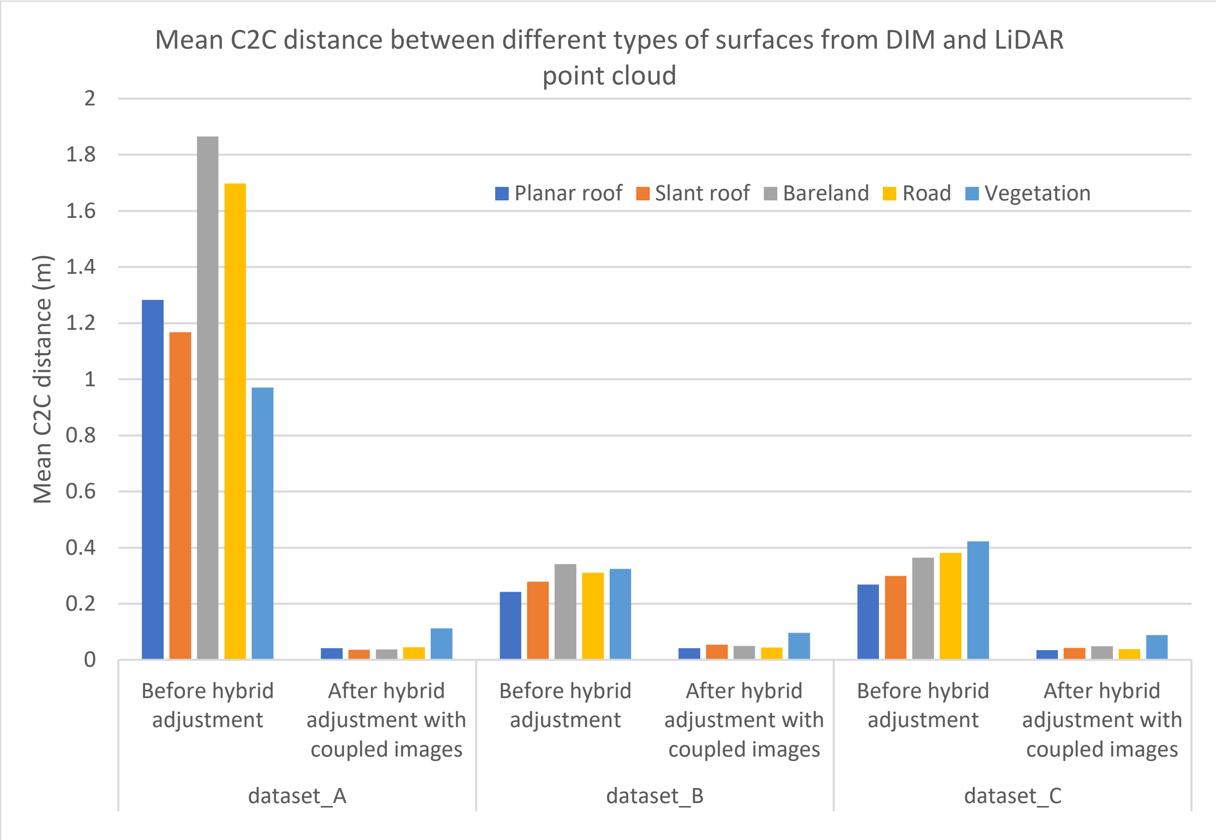


Figure 6.11: Bar plot representing mean C2C distance between different surfaces from dataset_A, dataset_B, and dataset_C

## 6.4. DSM-based height differences between LiDAR and DIM point clouds

We have also considered a secondary quality check with computation of DSM-based height differences to evaluate the performance of the hybrid adjustment approach. The relative height differences between the LiDAR and DIM point clouds were computed with the OPALS quality check module in which DSMs are computed for the point clouds, and their relative height differences are estimated. The height differences are computed simply as the raster subtraction of two DSMs from LiDAR and DIM point clouds. The mean height differences before and after hybrid adjustment are summarized in Table 6.7 and represented by a bar plot in Figure 6.12.

Table 6.7: Mean height differences between DSMs from LiDAR and DIM point cloud

| Dataset | Mean height differences (m) | |
|---|---|---|
| | Before hybrid adjustment | After hybrid adjustment |
| Dataset_A | 1.022 | 0.141 |
| Dataset_B | 0.252 | 0.102 |
| Dataset_C | 0.261 | 0.090 |

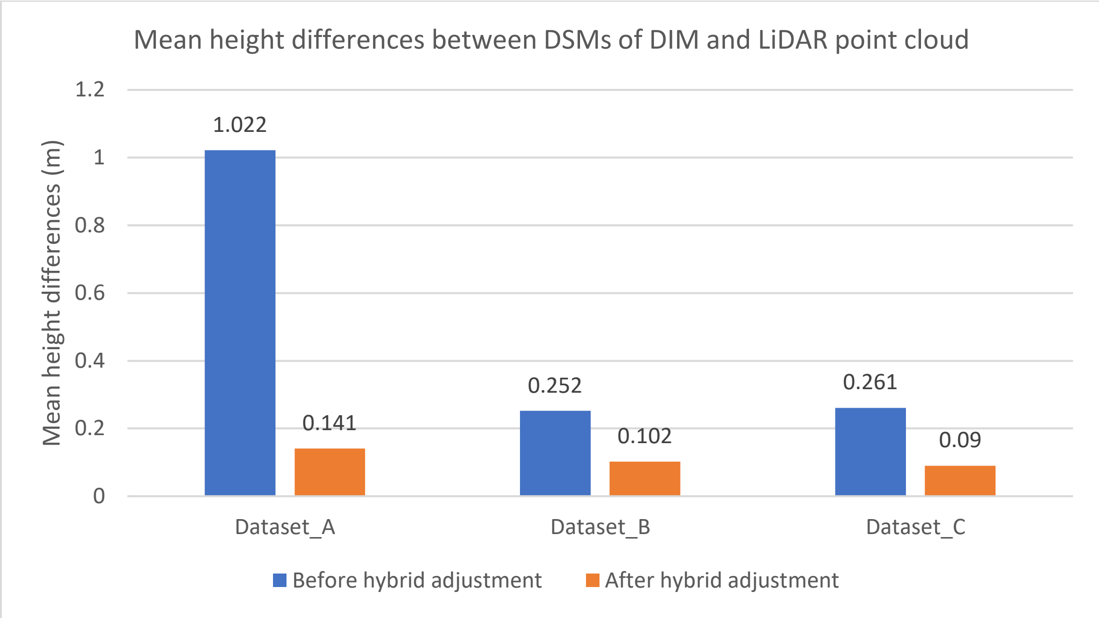


Figure 6.12: Bar plot showing mean height differences between DSMs of DIM and LiDAR point cloud

Figure 6.13 shows the relative height differences between DIM and LiDAR point clouds before hybrid adjustment (on the left) and after hybrid adjustment (on the right). It can be observed that the differences were higher than 0.20 m (corresponding to blue), which were reduced after hybrid adjustment indicated by regions corresponding to the lower differences scale values in Figure 6.13. The results for the mean height differences in Table 6.7 are supported by the visual representation of height differences in Figure 6.13.

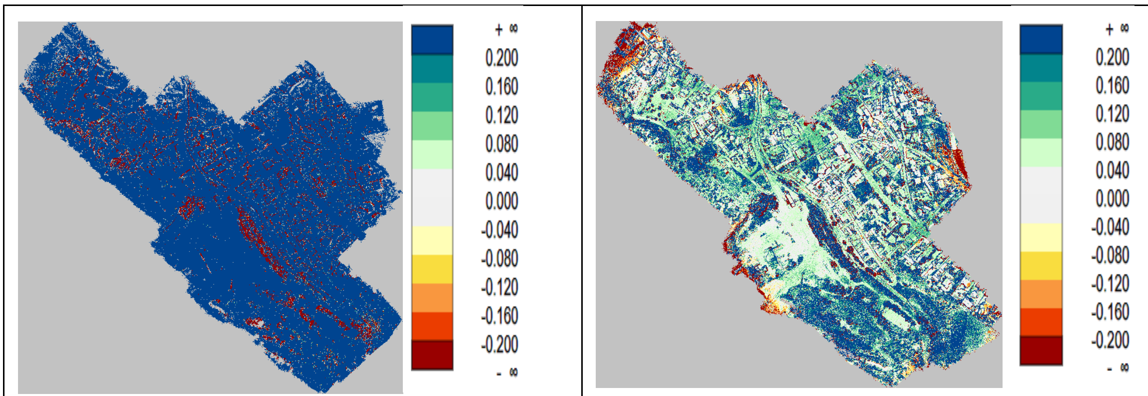


a) Before hybrid adjustment

b) After hybrid adjustment with coupled images

Figure 6.13: Relative height differences between DIM and LiDAR point clouds from dataset_A

The relative height differences between DIM and LiDAR point clouds from dataset_B are shown in Figure 6.14, indicating the improved orientation of both LiDAR and DIM point clouds post hybrid adjustment. The relative differences around the central and corner regions of dataset_B were initially above the 0.20 m range, which came down to a few centimeters level post hybrid adjustment.

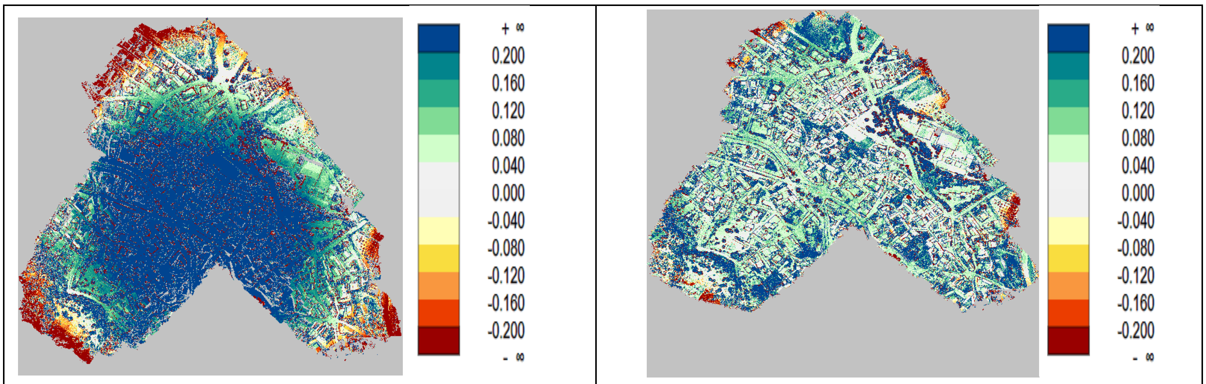


a) Before hybrid adjustment b) After hybrid adjustment with coupled images

Figure 6.14: Relative height differences between DIM and LiDAR point clouds from dataset_B

Similar to the dataset_A and dataset_C, the relative height differences for the LiDAR and DIM point clouds from dataset_C are shown in Figure 6.15. The relative differences were reduced in dataset_C as well after hybrid adjustment, which is represented in Figure 6.15.

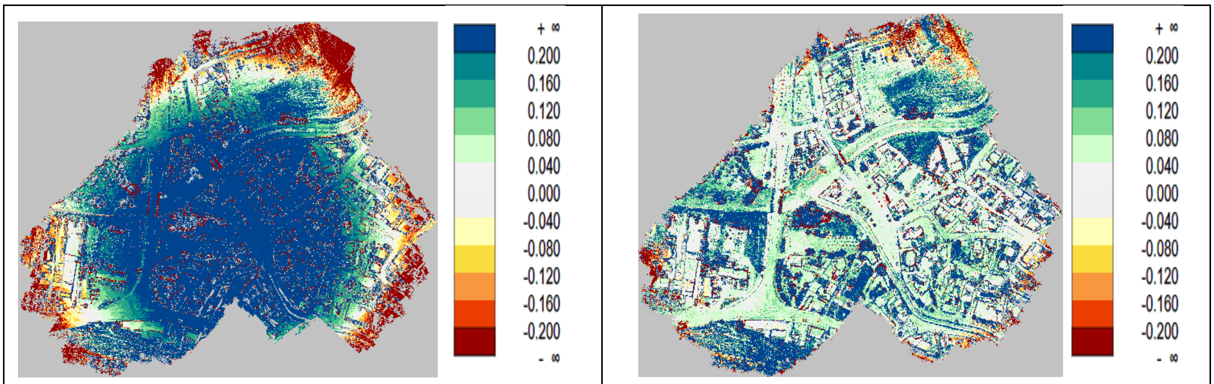


a) Before hybrid adjustment b) After hybrid adjustment with coupled images

Figure 6.15: Relative height differences between DIM and LiDAR point clouds from dataset_C

The analysis of the discrepancies between LiDAR and camera datasets with the computation of the mean height differences between DSMs of point clouds also indicates significant improvements in the orientation of the datasets post hybrid adjustment. The results from the computation of the DSM-based height differences are not exactly similar to Cloud-to-Cloud distances because DSM is a raster with a 2D representation of the elevation of the terrain, whereas point clouds are 3D models. Although, both C2C distances and relative height differences show a similar trend for the discrepancies before and after hybrid adjustment for all the three datasets. The DSM-based height difference is the raster subtraction of two DSMs derived from LiDAR and DIM point clouds, only considering the points on the top of the surfaces from both the point clouds.

# 7. CONCLUSIONS AND RECOMMENDATIONS

## 7.1. Conclusions

This research study aimed to find and implement a hybrid adjustment approach for the UAS-based LiDAR and image data. The purpose of the hybrid adjustment was to minimize the discrepancies or errors between the LiDAR point cloud and the image-based DIM point clouds, i.e., to minimize the distances between LiDAR and DIM point clouds. In the hybrid adjustment approach, the LiDAR strips were adjusted along with the camera images with an estimation of camera orientation parameters.

The hybrid adjustment approach was implemented in OPALS software with two cases for image data inputs: one is loose images, and another is coupled images. In the case of loose images, the exterior orientations of the camera are estimated in the adjustment itself. In contrast, in the case of adjustment with coupled images, the images are indexed to a strip, and their orientations are derived from mounting calibration parameters and UAS trajectory. Three datasets have been used in this research collected with the same UAS platform and sensors. The implementation time is almost similar for hybrid adjustment with loose and coupled images.

For the first dataset, hybrid adjustment approach experiments were carried out with both loose and coupled images. For the initial experimentation with the dataset_A, the hybrid adjustment approach was implemented with a bias and linear trajectory correction models to see their effect on the results of the hybrid adjustment. Based on the hybrid adjustment approach results from table 4 and figure 6.1, the hybrid adjustment with coupled images and bias trajectory correction model resulted in the most accurate orientation between the LiDAR and DIM point clouds. For the first quality check, the mean C2C distances between LiDAR and DIM point clouds were chosen to check the discrepancies in which lower mean C2C distances between point clouds indicate the better orientation of point clouds. For the dataset_A, the initial C2C distances between two-point clouds were in the range of meters (1.172 m), whereas after hybrid adjustment, the C2C distances were reduced to a sub-centimeter range (0.088 m/8.8 cm). Results from this experimentation (table 4 and figure 6.1) indicated that the simpler bias trajectory correction model gives a more accurate orientation of the point clouds after the hybrid adjustment. So, for the other datasets (dataset_B and dataset_C), the hybrid adjustment was implemented with coupled images and a bias trajectory correction model. For the dataset_B, the initial discrepancies were 0.268 m, and after adjustment, they came down to 0.085 m. For the dataset_C, the discrepancies before the adjustment were 0.483 m, and after-hybrid adjustment, they were reduced to 0.067 m. After the hybrid adjustment, the reduced mean C2C distances indicate the improved relative orientations of UAS-based LiDAR and image datasets. The lesser C2C distances between LiDAR and camera point will lead to more accurate coregistration of both clouds. With lesser C2C distances between LiDAR and DIM point clouds, the integrated product from both datasets is expected to be more accurate with the detailed information.

The mean C2C distances at the complete dataset level can give an inaccurate interpretation of the errors between the point clouds due to their different point density, penetrating capability of LiDAR, and different sensor characteristics. So, the surface level analysis of mean C2C distance was done for different surfaces, namely flat roof, slant roof, bare land, road, and vegetation for all three datasets. From the surface level analysis results in Figure 6.11, the discrepancies for different surfaces were also observed at sub-centimeter levels. It was observed that the mean C2C distances were smaller at the surface levels except for the vegetation surfaces as compared to the mean C2C distances for the complete dataset. The higher mean C2C distances for vegetation surfaces can be attributed to the penetration capability of LiDAR through the vegetation surfaces.

The mean height differences between DSMs of LiDAR and DIM point clouds were computed using the OpalsQuality module to check the discrepancies between point clouds. The results of the mean height differences from Table 6.7 and Figure 6.12 also support the performance of hybrid adjustment in minimizing the discrepancies between LiDAR and camera point clouds.

The results of the hybrid adjustment workflow in this research indicate that it can minimize the discrepancies between the LiDAR and image data from the range of meters to the sub-centimeter range without using any ground truth inputs. This adjustment workflow can be used in the applications for the mapping where sub-centimeter level accuracy is acceptable.

### 7.2. Advantages of the hybrid adjustment approach used in this research

- The hybrid adjustment approach simultaneously optimizes the relative as well the absolute orientation of the UAS-based LiDAR and image data
- Time-consuming measurements of LiDAR control planes are not required in adjustment as ground-based photogrammetric signals can be used as ground control (Norbert Haala et al., 2022)
- Hybrid adjustment gives the improved results in the order of average GSD even in the absence of any ground control points or control point clouds
- It automatically estimates the adjustment parameters for both image data and LiDAR strips
- Numerous applications in multiple modeling and mapping studies

### 7.3. Limitations of the approach

- The initial setup for the hybrid adjustment is challenging and time-consuming.
- Unless fully automated tools are developed for the hybrid adjustment, a sound understanding of programming and mathematical models would be required for the implementation of hybrid adjustment.
- As the StripAdjust module in Opals was originally designed for ALS data, the optimal parameters for hybrid adjustment of the UAS-based datasets can only be obtained through hit-and-trial experimentation or a high level of expertise in this field.

### 7.4. Recommendations for the further studies

- Ground Control inputs (GCPs or CPCs) can be used in the hybrid adjustment to improve the accuracy of the hybrid adjustment approach.
- The experiment with a lower threshold point-to-plane distance can be tested to see how the adjustment converges or minimizes the errors.
- The constraints like planarity and roughness values can be added to inputs to improvise the results of hybrid adjustment.
- Modeling the relation between distances of camera and LiDAR sensors mounted on a UAS system in a geometric constraint within the hybrid adjustment can also be investigated to improve the results further.

## 7.5. Answers to the research questions

- Research question 1: What is the hybrid adjustment process, and what inputs and optimal parameters need to be considered for the hybrid adjustment of UAS-based LiDAR and image data?

  The hybrid adjustment approach is a workflow that simultaneously optimizes the relative and absolute orientation of LiDAR and image data to minimize the discrepancies/errors associated with them. For the hybrid adjustment in software Opals, the required inputs are LiDAR measurements, image tie points, orientations of the images, and the trajectory of the UAS system. The optimal parameters for the hybrid adjustment have been obtained through multiple experiments with data subsets, and the optimal ones are used for hybrid adjustment with complete datasets. The parameters used in the hybrid adjustment with loose and coupled images can be found in Appendix B.

- Research question 2: What are loose and coupled images, and what is their role in the implementation of the hybrid adjustment process?

  In the case of loose images, their relation to flight trajectory cannot be established because of the unavailability of timestamps for images. The camera is not connected to the trajectory in the case of loose images. In this case, the exterior orientation parameters are directly estimated by the adjustment. In the case of coupled images, the images are tied to the trajectory through the image time stamps. Every image is indexed to a strip according to the GPS time. The exterior orientation of the images can be estimated through a direct georeferencing equation as a function of UAS trajectory and camera mounting calibration parameters. In both cases of hybrid adjustment with the loose and coupled images, the image tie points and object point observations are used in the hybrid adjustment as inputs, and the point-to-plane distances for image tie points and LiDAR strips and reprojection error have been minimized in the final adjustment step.

- Research question 3: Which types of correspondences are established, and how are they established in the hybrid adjustment process?

  Three types of correspondences have been used in the hybrid adjustment approach. The first one is between image pairs (IMG-IMG), which are established with SIFT algorithm to find the common features in the overlapping images. The second type of correspondence is between overlapping LiDAR strips (STR-STR) established by the selection, matching, and rejection steps from the modified ICP algorithm. A single STR-STR correspondence is two points from overlapping LiDAR strips and their normal vectors estimated from the neighboring points. The third type of correspondence is between image tie points and overlapping LiDAR strips (IMG-STR), which are established between the overlap area of UAS-based images and LiDAR strip. The IMG-STR correspondences are established similarly to STR-STR correspondences by selecting, matching, and rejection steps based on the modified ICP algorithm.

- Research question 4: What constraints can be applied to the establishment of the correspondence in the hybrid adjustment approach, and how do these constraints affect the hybrid adjustment process?

  The constraints for the roughness and angle between normal vectors of the corresponding points can be used in the hybrid adjustment approach. The corresponding points in the similar normal vector directions are more reliable and would result in the selection of the points from the same surface. Therefore, a small delta angle constraint has been used in the hybrid adjustment to only use the correspondences from the same surfaces only. An additional constraint is the roughness of the terrain/surface. The smoother surfaces would have more reliable normal vectors from the corresponding points, and so, more precise will be the point-to-plane distances which are to be minimized in the hybrid adjustment. So, adding the constraints of roughness and small delta angle to the hybrid adjustment would result in the accurate establishment of the correspondences and the outcomes with better accuracy.

- Research question 5: How does a trajectory correction model affect the hybrid adjustment process, and where does it play a role?

  The function of the trajectory correction model is to provide a smooth and continuous trajectory throughout the time and correct with a polynomial. In the case of the bias trajectory correction model, a constant value for the correction (bias) is estimated from the adjustment for the correction in the trajectory. In the case of a linear trajectory correction model, the correction in the trajectory follows a linear trend and is added to the original trajectory values for the correction. The UAS trajectory plays a central role in the hybrid adjustment approach. In the case of hybrid adjustment with coupled images, the exterior orientation parameters are estimated in the adjustment as a function of the UAS trajectory.

- Research question 6: Can the discrepancies be impacted by implementing the hybrid adjustment with loose and coupled images, and to what extent are they impacted?

  From the overall results of the hybrid adjustment with mean C2C distances quality check and mean height differences, it is clear that the hybrid adjustment approach can minimize the discrepancies between UAS-based LiDAR and camera data. The overall performance of the hybrid adjustment was investigated with loose and coupled images in combination with bias and linear trajectory correction models. The results of the hybrid adjustment implementation from Table 6.1 indicates that the hybrid adjustment with the coupled images and bias trajectory correction model gives the most accurate relative orientation between LiDAR and image data. From the hybrid adjustment with both loose and coupled images, the discrepancies between LiDAR and image data have been reduced from the range of meters to a few centimeters, but coupled images give relatively better results than loose images. So, hybrid adjustment with coupled images is recommended to achieve an accurate coregistration between the point clouds from LiDAR and image data.

# 8. ETHICAL CONSIDERATIONS

1. The dataset (s) for this M.Sc. research work were acquired by Alto-drones and provided by the scientific advisor Dr. Fabio Remondino, FBK, Trento, Italy
2. Dataset(s) used in this research work were used with the consent of the data owner and are not open source.
3. Opals was used with an academic license key provided by team Opals, Technical University in Wien, to implement the hybrid adjustment.
4. The central methodology and mathematical framework for this research work have been adopted from the Ph.D. work of Dr. Philipp Glira at Technical University in Wien

# LIST OF REFERENCES


Abayowa, B. O., Yilmaz, A., & Hardie, R. C. (2015). Automatic registration of optical aerial imagery to a LiDAR point cloud for generation of city models. *ISPRS Journal of Photogrammetry and Remote Sensing*, *106*, 68–81. https://doi.org/10.1016/j.isprsjprs.2015.05.006

Ahmad Fuad, N., Yusoff, A. R., Ismail, Z., & Majid, Z. (2018). Comparing the performance of point cloud registration methods for landslide monitoring using mobile laser scanning data. *International Archives of the Photogrammetry, Remote Sensing and Spatial Information Sciences - ISPRS Archives*, *42*(4/W9), 11–21. https://doi.org/10.5194/isprs-archives-XLII-4-W9-11-2018

Almqvist, H., Magnusson, M., Kucner, T. P., & Lilienthal, A. J. (2018). Learning to detect misaligned point clouds. *Journal of Field Robotics*, *35*(5), 662–677. https://doi.org/10.1002/rob.21768

Alto-drones. (2021). *alto-drones*. https://doi.org/https://www.alto-drones.com/

Ayman Habib. (2018). Topographic Laser Ranging and Scanning Principles and Processing, Second Edition. In C. K. T. Jie Shan (Ed.), *Topographic Laser Ranging and Scanning Principles and Processing, Second Edition* (Second). CRC Press.

Baltsavias, E. P. (1999). A comparison between photogrammetry and laser scanning. *ISPRS Journal of Photogrammetry and Remote Sensing*, *54*(2–3), 83–94. https://doi.org/10.1016/S0924-2716(99)00014-3

Bäumker, M., & Heimes, F. (2002). New Calibration and Computing Method for Direct Georeferencing of Image and Scanner Data Using the Position and Angular Data of an Hybrid Inertial Navigation System. *Proceedings of OEEPE Workshop on Integrated Sensor Orientation*.

Beger, R., Gedrange, C., Hecht, R., & Neubert, M. (2011). Data fusion of extremely high resolution aerial imagery and LiDAR data for automated railroad centre line reconstruction. *ISPRS Journal of Photogrammetry and Remote Sensing*, *66*(6), S40–S51. https://doi.org/10.1016/j.isprsjprs.2011.09.012

Besl, P. J., & McKay, N. D. (1992). A method for registration of 3-D shapes. *IEEE Transactions on Pattern Analysis and Machine Intelligence*, *14*(2), 239–256. https://doi.org/10.1109/34.121791

Brenner, C. (2005). Building reconstruction from images and laser scanning. *International Journal of Applied Earth Observation and Geoinformation*, *6*(3–4), 187–198. https://doi.org/10.1016/j.jag.2004.10.006

Chen, Y., & Medioni, G. (1992). Object modelling by registration of multiple range images. *Image and Vision Computing*, *10*(3), 145–155. https://doi.org/https://doi.org/10.1016/0262-8856(92)90066-C

Chen, Y., & Medioni, G. G. (1991). Object modeling by registration of multiple range images. *Proceedings. 1991 IEEE International Conference on Robotics and Automation*, 2724–2729 vol.3.

Choi, K., Hong, J., & Lee, I. (2011). Precise geometric registration of aerial imagery and LIDAR data. *ETRI Journal*, *33*(4), 506–516. https://doi.org/10.4218/etrij.11.1610.0046

CloudCompare. (2021). *Distances Computation*. https://www.cloudcompare.org/doc/wiki/index.php/Distances_Computation

Cucchiaro, S., Fallu, D. J., Zhang, H., Walsh, K., Oost, K. Van, Brown, A. G., & Tarolli, P. (2020). Multiplatform-SfM and TLS data fusion for monitoring agricultural terraces in complex topographic and landcover conditions. *Remote Sensing*, *12*(12). https://doi.org/10.3390/rs12121946

Förstner, W., & Wrobel, B. P. (2016). Bundle Adjustment. In *Photogrammetric Computer Vision: Statistics, Geometry, Orientation and Reconstruction* (pp. 643–725). Springer International Publishing. https://doi.org/10.1007/978-3-319-11550-4_15

Fritz, A., Kattenborn, T., & Koch, B. (2013). UAV-BASED PHOTOGRAMMETRIC POINT CLOUDS – TREE STEM MAPPING IN OPEN STANDS IN COMPARISON TO TERRESTRIAL LASER SCANNER POINT CLOUDS. *The International Archives of the Photogrammetry, Remote Sensing and Spatial Information Sciences*, *XL-1/W2*, 141–146. https://doi.org/10.5194/isprsarchives-XL-1-W2-141-2013

GeoCue Group. (2021). *True View 3D Imaging Systems Fly, Collect, Process, Deliver*. https://geocue.com/products/3d-imaging-systems-true-view/

Gerum, R. C., Richter, S., Winterl, A., Mark, C., Fabry, B., Le Bohec, C., & Zitterbart, D. P. (2019). CameraTransform: A Python package for perspective corrections and image mapping. *SoftwareX*, *10*, 100333. https://doi.org/https://doi.org/10.1016/j.softx.2019.100333

Glira, P, Pfeifer, N., & Mandlburger, G. (2019). HYBRID ORIENTATION OF AIRBORNE LIDAR POINT CLOUDS AND AERIAL IMAGES. *ISPRS Annals of the Photogrammetry, Remote Sensing and Spatial Information Sciences*, *IV-2/W5*, 567–574. https://doi.org/10.5194/isprs-annals-IV-2-W5-567-2019

Glira, Philipp. (2018). *Hybrid Orientation of LiDAR Point Clouds and Aerial Images Hybride Orientierung von Laserscanning-Punktwolken und Luftbildern*.
Glira, Philipp, PfeifeR, N., Briese, C., & ReSSl, C. (2015). A correspondence framework for ALS strip adjustments based on variants of the ICP algorithm. *Photogrammetrie, Fernerkundung, Geoinformation*, *2015*(4), 275–289. https://doi.org/10.1127/pfg/2015/0270
Gomez, C., & Purdie, H. (2016). UAV- based Photogrammetry and Geocomputing for Hazards and Disaster Risk Monitoring – A Review. *Geoenvironmental Disasters*, *3*(1). https://doi.org/10.1186/s40677-016-0060-y
Haala, N., Kölle, M., Cramer, M., Laupheimer, D., Mandlburger, G., & Glira, P. (2020). Hybrid Georeferencing, Enhancement and Classification of Ultra-High Resolution Uav Lidar and Image Point Clouds for Monitoring Applications. *ISPRS Annals of the Photogrammetry, Remote Sensing and Spatial Information Sciences*, *5*(2), 727–734. https://doi.org/10.5194/isprs-annals-V-2-2020-727-2020
Haala, Norbert, Kölle, M., Cramer, M., Laupheimer, D., & Zimmermann, F. (2022). Hybrid georeferencing of images and LiDAR data for UAV-based point cloud collection at millimetre accuracy. *ISPRS Open Journal of Photogrammetry and Remote Sensing*, *4*, 100014. https://doi.org/https://doi.org/10.1016/j.ophoto.2022.100014
Habib, A, Ghanma, M., & Kim, E. (2005). LIDAR Data for Photogrammetric Georeferencing. *Proc. FIG Working Week and GSDI-8*, 15. https://www.fig.net/resources/proceedings/fig_proceedings/cairo/papers/ts_38/ts38_04_habib_etal.pdf
Habib, Ayman, Ghanma, M., Morgan, M., & Al-Ruzouq, R. (2005). Photogrammetric and lidar data registration using linear features. *Photogrammetric Engineering and Remote Sensing*, *71*(6), 699–707. https://doi.org/10.14358/PERS.71.6.699
Haklay, M., & Weber, P. (2008). OpenStreet map: User-generated street maps. *IEEE Pervasive Comput.*, *7*(4), 12–18. https://doi.org/10.1109/MPRV.2008.80
Hebel, M., & Stilla, U. (2012). Simultaneous Calibration of ALS Systems and Alignment of Multiview LiDAR Scans of Urban Areas. *IEEE Transactions on Geoscience and Remote Sensing*, *50*(6), 2364–2379. https://doi.org/10.1109/TGRS.2011.2171974
Horn, B. K. P. (1987). Closed-form solution of absolute orientation using unit quaternions. *Journal of the Optical Society of America A*, *4*(4), 629. https://doi.org/10.1364/josaa.4.000629
IGI Systems. (2022). *IGI systems*. https://www.igi-systems.com/home.html
Jie Shan, C. K. T. (2018). *Topographic Laser Ranging and Scanning Principles and Processing, Second Edition* (C. K. T. Jie Shan (ed.); Second). CRC Press.
Kerle, N., Nex, F., Gerke, M., Duarte, D., & Vetrivel, A. (2020). UAV-Based Structural Damage Mapping: A Review. *ISPRS International Journal of Geo-Information*, *9*(1). https://doi.org/10.3390/ijgi9010014
Kim, C., Ghanma, M., & Habib, A. (2006). Integration of Photogrammetric and LIDAR Data for Realistic 3D Model Generation surfaces Direct acquisition of 3D coordinates Photogrammetric Cons Almost no positional information along homogeneous surfaces Complicated and sometimes unreliable Vertical ac. *Environmental Engineering*.
Kumar Mishra, R. (2012). A Review of Optical Imagery and Airborne LiDAR Data Registration Methods. *The Open Remote Sensing Journal*, *5*(1), 54–63. https://doi.org/10.2174/1875413901205010054
Laser Interferometer Gravitational-Wave Observatory. (2022). *LiGO*. https://doi.org/https://www.andrews.edu/~tzs/timeconv/timedisplay.php
Leica Geosystems. (2022). *Leica CityMapper-2*. https://leica-geosystems.com/products/airborne-systems/leica-citymapper-2
Lin, Y.-C., & Habib, A. (2021). Quality control and crop characterization framework for multi-temporal UAV LiDAR data over mechanized agricultural fields. *Remote Sensing of Environment*, *256*, 112299. https://doi.org/https://doi.org/10.1016/j.rse.2021.112299
Mandlburger, G., Wenzel, K., Spitzer, A., Haala, N., Glira, P., & Pfeifer, N. (2017). IMPROVED TOPOGRAPHIC MODELS VIA CONCURRENT AIRBORNE LIDAR AND DENSE IMAGE MATCHING. *ISPRS Annals of the Photogrammetry, Remote Sensing and Spatial Information Sciences*, *IV-2/W4*, 259–266. https://doi.org/10.5194/isprs-annals-IV-2-W4-259-2017
MATLAB. (2021). *Camera calibration*. https://nl.mathworks.com/help/vision/ug/camera-calibration.html
Moasaic. (2022). *Mosaic*. https://www.mosaic51.com/technology/lidar-vs-photogrammetry-which-is-better-for-point-cloud-creation/

Nex, F., Armenakis, C., Cramer, M., Cucci, D. A., Gerke, M., Honkavaara, E., Kukko, A., Persello, C., & Skaloud, J. (2022). UAV in the advent of the twenties: Where we stand and what is next. *ISPRS Journal of Photogrammetry and Remote Sensing*, *184*(January), 215–242. https://doi.org/10.1016/j.isprsjprs.2021.12.006

Palenichka, R. M., & Zaremba, M. B. (2010). Automatic extraction of control points for the registration of optical satellite and LiDAR images. *IEEE Transactions on Geoscience and Remote Sensing*, *48*(7), 2864–2879. https://doi.org/10.1109/TGRS.2010.2043677

Pandey, A., Chaube, U. C., Mishra, S. K., & Kumar, D. (2016). Assessment of reservoir sedimentation using remote sensing and recommendations for desilting Patratu Reservoir, India. *Hydrological Sciences Journal*, *61*(4), 711–718. https://doi.org/10.1080/02626667.2014.993988

Peng, S., Ma, H., & Zhang, L. (2019). Automatic registration of optical images with airborne liDAR point cloud in urban scenes based on line-point similarity invariant and extended collinearity equations. *Sensors (Switzerland)*, *19*(5). https://doi.org/10.3390/s19051086

Pentek, Q., Kennel, P., Allouis, T., Fiorio, C., & Strauss, O. (2020). A flexible targetless LiDAR–GNSS/INS–camera calibration method for UAV platforms. *ISPRS Journal of Photogrammetry and Remote Sensing*, *166*(May), 294–307. https://doi.org/10.1016/j.isprsjprs.2020.05.014

Pfeifer, N., Mandlburger, G., Otepka, J., & Karel, W. (2014). OPALS – A framework for Airborne Laser Scanning data analysis. *Computers, Environment and Urban Systems*, *45*, 125–136. https://doi.org/https://doi.org/10.1016/j.compenvurbsys.2013.11.002

Ressl, C., Brockmann, H., Mandlburger, G., & Pfeifer, N. (2016). Dense Image Matching vs. Airborne Laser Scanning ? Comparison of two methods for deriving terrain models. *Photogrammetrie - Fernerkundung - Geoinformation*, *2016*(2), 57–73. https://doi.org/10.1127/pfg/2016/0288

Ribeiro, L. G. (2021). *3D Reconstruction of Civil Infrastructures from UAV Lidar point clouds*.

RIEGL. (2022). *RIEGL miniVUX-3UAV*. https://doi.org/http://www.riegl.com/products/unmanned-scanning/riegl-minivux-3uav/

Shakarji, C. M. (1998). Least-Squares Fitting Algorithms of the NIST Algorithm Testing System. *Journal of Research of the National Institute of Standards and Technology*, *103*(6), 633–641. https://doi.org/10.6028/jres.103.043

Skaloud, J. (2006). *Reliability of Direct Georeferencing Phase 1: An Overview of the Current Approaches and Possibilities., Checking and Improving of Digital Terrain Models / Reliability of Direct Georeferencing.*

Skaloud, Jan, & Lichti, D. (2006). Rigorous approach to bore-sight self-calibration in airborne laser scanning. *ISPRS Journal of Photogrammetry and Remote Sensing*, *61*(1), 47–59. https://doi.org/https://doi.org/10.1016/j.isprsjprs.2006.07.003

Skaloud, Jan, Schaer, P., Stebler, Y., & Tomé, P. (2010). Real-time registration of airborne laser data with sub-decimeter accuracy. *ISPRS Journal of Photogrammetry and Remote Sensing*, *65*(2), 208–217. https://doi.org/10.1016/j.isprsjprs.2009.12.003

SONY. (2022). *SONY ILCE-7RM3*. https://doi.org/https://www.sony.nl/electronics/cameras-met-verwisselbare-lens/ilce-7rm3/specifications

Toschi, I., Farella, E. M., Welponer, M., & Remondino, F. (2021). Quality-based registration refinement of airborne LiDAR and photogrammetric point clouds. *ISPRS Journal of Photogrammetry and Remote Sensing*, *172*(December 2020), 160–170. https://doi.org/10.1016/j.isprsjprs.2020.12.005

Toschi, I., Remondino, F., Rothe, R., & Klimek, K. (2018). Combining airborne oblique camera and LiDAR sensors: Investigation and new perspectives. *International Archives of the Photogrammetry, Remote Sensing and Spatial Information Sciences - ISPRS Archives*, *42*(1), 437–444. https://doi.org/10.5194/isprs-archives-XLII-1-437-2018

Vilbig, J. M., Sagan, V., & Bodine, C. (2020). Archaeological surveying with airborne LiDAR and UAV photogrammetry: A comparative analysis at Cahokia Mounds. *Journal of Archaeological Science: Reports*, *33*, 102509. https://doi.org/https://doi.org/10.1016/j.jasrep.2020.102509

Wallace, L., Lucieer, A., Watson, C., & Turner, D. (2012). Development of a UAV-LiDAR System with Application to Forest Inventory. *Remote Sensing*, *4*(6), 1519–1543. https://doi.org/10.3390/rs4061519

Wei, R. (2017). Research on optimized land use structure of kunming under the concept of smart city-analysis based on big data of urban development. *Proceedings - 2016 International Conference on Intelligent Transportation, Big Data and Smart City, ICITBS 2016*, 155–158. https://doi.org/10.1109/ICITBS.2016.49

Yang, B., & Chen, C. (2015). Automatic registration of UAV-borne sequent images and LiDAR data. *ISPRS Journal of Photogrammetry and Remote Sensing*, *101*, 262–274. https://doi.org/10.1016/j.isprsjprs.2014.12.025

YellowScan. (2020). *YellowScan*. https://www.yellowscan-lidar.com/uav-lidar-integration/

Zhang, J. (2010). Multi-source remote sensing data fusion: status and trends. *International Journal of Image and Data Fusion*, *1*(1), 5–24. https://doi.org/10.1080/19479830903561035

Zhang, J., & Lin, X. (2017). Advances in fusion of optical imagery and LiDAR point cloud applied to photogrammetry and remote sensing. *International Journal of Image and Data Fusion*, *8*(1), 1–31. https://doi.org/10.1080/19479832.2016.1160960

Zhou, G., & Reichle, S. (2010). UAV-based multi-sensor data fusion processing. *International Journal of Image and Data Fusion*, *1*(3), 283–291. https://doi.org/10.1080/19479832.2010.497343

Zhou, T., Hasheminasab, S. M., & Habib, A. (2021). Tightly-coupled camera/LiDAR integration for point cloud generation from GNSS/INS-assisted UAV mapping systems. *ISPRS Journal of Photogrammetry and Remote Sensing*, *180*(May), 336–356. https://doi.org/10.1016/j.isprsjprs.2021.08.020

# APPENDICES

**Appendix A: Python script and the parameters used to transform the outputs from Agisoft Metashape script into input for Opals stripAdjust**

Python metaShape2stripAdjust.py -project path () -chunk () -maxReprojection error () -minMultiplicity () -warnIfLessImagePointsThan () -outDir Path ()

Table 9.1: Parameters used in python script to transform Agisoft Metashape project into input for Opals StripAdjust

| Parameters | Values used for dataset_A | Values used for dataset_B | Values used for dataset_C |
|---|---|---|---|
| Chunk | 0 | 0 | 0 |
| maxReprojectionError | 0.878 | 0.840 | 0.861 |
| minMultiplicity | 4 | 4 | 4 |
| warnIfLessImagePointsThan | 20 | 20 | 20 |

**Appendix B: Parameters and values used in hybrid adjustment with loose and coupled images**

Table 9.2: Parameters and values used in the hybrid adjustment

| Parameters | Values used |
|---|---|
| UTM Zone | 32N |
| UTM Hemisphere | North |
| Voxel Size | 5 |
| No. of iterations | 5 |
| Scanner orientation | urf |
| trajectory correction model | bias |
| Trajectory time sampling interval (seconds) | 10 |
| trajectory standard deviation of direct observations | 0 (constant value) |
| strips.normals.searchRadius (Search radius for plane fitting)_ | 1.5 |
| strips.normals.neighbours (min no neighbors for normal estimation) | 8 |
| strips.normals.subsetRadius (Radius for subset areas) | 3 |
| trajectory.timelag | (-) 18 secs |
| images.all.extOri.X0.sigmaApriori (standard deviation of observations) | 0.2 |
| C (focal length) (in pixels) | 4771.2 |
| Principal point (X) (in pixels) | 3976 |
| Principal point (Y) (in pixels) | -2652 |
| lens distortion normalization radius (regulatory parameter) | 3000 |
| strip2strip.overlap (Minimum number of overlapping voxels) | 1 |
| strip2strip.selection.samplingDist ( sampling distance for subset point selection) | 5 |
| strip2strip.rejection.maxDist (Threshold distance between corresponding points) | 2 |
| Imgae2strip.dpSigPriori (priori point- to-plane distance between image tie points and LiDAR strips) | 0.5 |
| strAdj.cameras.all.xSigPriori (Standard deviation of image observations) | 0.5 |
| strAdj.cameras.all.ySigPriori<br>(Standard deviation of image observations) | 0.5 |
| image2strip.weighting.byDeltaAngle (Weight to normal vector directions) | True (1) |
| image2strip.weighting.byRoughness (Weight to surface roughness) | True (1) |
| image2image.minImageCount (min no of images for a observed tie point) | 3 |